Quantitative detection of grey and white matter amyloid pathology using a combination of K114 and CRANAD-3 fluorescence

Anastasiia A. Stepanchuk [a], Philip A. Barber [a], Tammaryn Lashley [b,c], Jeffrey T. Joseph [a,d], Peter K. Stys [a,*]

[a] Department of Clinical Neurosciences, Hotchkiss Brain Institute, University of Calgary, Cumming School of Medicine, Calgary, AB, Canada
[b] Department of Neurodegenerative Disease, UCL Queen Square Institute of Neurology, London, UK
[c] Queen Square Brain Bank for Neurological Disorders, Department of Clinical and Movement Neuroscience, UCL Queen Square Institute of Neurology, London, UK
[d] Department of Pathology and Laboratory Medicine, Alberta Health Services, Calgary, AB, Canada

ARTICLE INFO

ABSTRACT

Background: Alzheimer's disease (AD) is a neurodegenerative disease that exacts a huge toll on the patient, the healthcare system and society in general. Abundance and morphology of protein aggregates such as amyloid β plaques and tau tangles, along with cortical atrophy and gliosis are used as measures to assess the changes in the brain induced by the disease. Not all of these parameters have a direct correlation with cognitive decline. Studies have shown that only particular protein conformers can be the main drivers of disease progression, and conventional approaches are unable to distinguish different conformations of disease-relevant proteins.
Methods and results: Using the fluorescent amyloid probes K114 and CRANAD-3 and spectral confocal microscopy, we examined formalin-fixed paraffin-embedded brain samples from different control and AD cases. Based on the emission spectra of the probes used in this study, we found that certain spectral signatures can be correlated with different aggregates formed by different proteins. The combination of spectral imaging and advanced image analysis tools allowed us to detect variability of protein deposits across the samples.
Conclusion: Our proposed method offers a quicker and easier neuropathological assessment of tissue samples, as well as introducing an additional parameter by which protein aggregates can be discriminated.

1. Introduction

In the past two decades the hypothesis proposing amyloid plaques as the main drivers of AD has been challenged, based in part on the failure of clinical trials testing drugs designed to remove these deposits (Reitz, 2012; Vaz and Silvestre, 2020). Recent data instead suggest that low molecular weight assemblies in the presymptomatic stages of disease might contribute to or trigger initial neurodegeneration (Cline et al., 2018; Sengupta et al., 2016; Esparza et al., 2013). In addition, there is mounting evidence supporting the idea that amyloid β (Aβ) and tau might have prion-like properties, whereby misfolded species template their conformations onto naïve proteins, causing not only a loss of physiological function, but also a gain of toxic function by these improperly folded morphotypes (Langer et al., 2011; Holmes and Diamond, 2014; Meyer-Luehmann et al., 2006; Gaspar et al., 2010). It was shown that certain types of misfolded Aβ and tau aggregates exhibit higher levels of neurotoxicity, and can cause different deficits in brain cell function, supporting strain variability of proteins involved in AD progression (Condello et al., 2018; Aoyagi et al., 2019; Fändrich et al., 2018).

Detection of misfolded states of tau and Aβ, along with discrimination of different misfolded conformers of these proteins early in the disease course has been the focus of intense research, as this could help shed light on the earliest pathophysiological stages of the disease. The methods that are widely used for protein aggregation assessment in tissue at post-mortem analysis do not present an adequate solution to this challenge; routine neuropathological examination of human brains employ methods that have a limited ability to distinguish different types of aggregates formed by the same protein. Immunohistochemistry (IHC) is a well-established staining technique, but in general only reports the presence of a protein, without regard to its folding state, that is now known to be critical for pathogenesis of a variety of diseases.

Staining of brain sections with small organic molecules that preferentially bind to β-sheet-rich protein deposits were introduced at the

* Corresponding author.
  E-mail address: pstys@ucalgary.ca (P.K. Stys).

beginning of the 20th century with the textile dye Congo Red. Detection of Alzheimer's amyloid plaques and neurofibrillary tangles by this dye is typically based on its birefringence induced after binding to highly ordered protein aggregates (Howie and Brewer, 2009; Howie et al., 2008; Howie and Owen-Casey, 2010). Since the introduction of Congo Red, multiple classes of dyes have been synthesized to improve sensitivity and specificity of such staining approaches; when contacting amyloid the majority of probes described to date, rather than inducing birefringence into the image, instead exhibit a change in fluorescence properties, such as increased quantum yield, shifts in excitation and emission spectra and alterations of fluorescence lifetime (Aliyan et al., 2019). Compared to immunohistochemistry, the mechanisms that govern the binding of amyloid probes to protein aggregates are highly dependent on the structure of both the dye molecule and the aggregate itself. For example, docking of the thioflavin T molecule to restricted hydrophobic pockets between peptide chains of the β sheet reduces its internal molecular rotation thereby increasing fluorescence quantum yield and therefore brightness, with little change in shape of emission spectrum (Khurana et al., 2005; Biancalana and Koide, 2010). In contrast, certain dyes, such as luminescent conjugated oligothiophenes, were shown to change emission spectrum depending on the structure of the protein aggregate to which they bind (Aslund et al., 2009; Nilsson et al., 2018; Sigurdson et al., 2007).

K114 ((trans,trans)-1-bromo-2,5-bis(4-hydroxystyryl)benzene) is a Congo Red derivative that was shown to bind to aggregates formed by Aβ, tau and alpha synuclein (Crystal et al., 2003; Levine, 2005; Burré et al., 2015). As we have recently shown (Stepanchuk et al., 2021), owing to the presence of titratable phenol rings in its structure, the change in K114 emission spectrum is able to report different types of amyloids by shifts in emission spectrum. Another fluorescent amyloid probe, CRANAD-3 is a derivative of curcumin, capable of detecting different species of Aβ assemblies with high affinity (Zhang et al., 2015). Though both fluorophores were previously reported to have amyloid-binding properties, the mechanisms of their interactions with protein aggregates are not precisely understood. Due to significantly different chemical structures of these two dyes, we posited that the potentially distinct mechanisms of reporting amyloid deposition would allow for a more complete detection of protein aggregates and better strain discrimination. In addition, distinct excitation and emission spectra of K114 and CRANAD-3 made it possible to differentiate between the signal originating from each dye. Here we combine these two probes from different classes in a single staining to examine amyloid pathology in human samples and cross-validate the amyloid staining by immunohistochemistry. We found that our approach not only reduced the number of steps required to detect Aβ and tau aggregates compared to immunochemical techniques, but also provided more information about conformational variability of protein deposits. Using advanced spectral analysis tools, we were able to characterize and distinguish the aggregates of the same protein based on different emission signatures. Taken together, our method has significant potential to augment existing techniques of histological tissue examination, providing more detail about accumulation of protein aggregates in a time- and cost-effective manner.

2. Materials and methods

2.1. Reagents

Dimethyl sulfoxide (DMSO), Na_2CO_3, Tween-20, formic acid (95–97%) and glycerol were obtained from Sigma-Aldrich (St. Louis, MO). K114 was purchased from Tocris Inc. (Fremont, CA). Stock solution of K114 (5 mM) was prepared in DMSO. CRANAD-3 was synthesized in house and stored as a 10 mM stock solution in 100% ethanol. Both dye stock solutions were stored at +4 °C. Mouse anti-Aβ antibody (1–16, clone 6E10), was purchased from Covance (Princeton, NJ, cat. number SIG-39320) and rabbit pan-tau antibody K9JA was from Agilent

(Santa Clara, CA, cat. number A002401-2). Goat anti-mouse Alexa Fluor 488 was acquired from Thermo Fisher Scientific (Waltham, MA, cat. number A-11029) and donkey anti-rabbit Alexa Fluor 594 secondary antibody was purchased from Jackson ImmunoResearch (West Grove, PA, code 711-895-152). Normal goat serum and bovine serine albumin, as well as Fluoromount were obtained from Sigma-Aldrich (St. Louis, MO, cat. numbers G 9023, A 2153 and F 4680 respectively).

2.2. Human tissue selection

Formalin-fixed, paraffin-embedded tissue samples were obtained from 6 AD patients and 6 cognitively normal control cases. All samples were obtained through the brain donation program of the Queen Square Brain Bank for Neurological disorders, UCL. The ApoE status was obtained as described previously (Toomey et al., 2020). Six μm thick brain sections of anterior cingulate, temporal cortex and hippocampus were used for amyloid probe staining and subsequently immunohistochemistry. Alpha-synuclein pathology was assessed using the current diagnostic criteria (Attems et al., 2021), four cases were found to fulfil the diagnostic criteria for neocortical pathology. One case only contained Lewy bodies in the amygdala and the remaining case was negative for alpha-synuclein pathology. TDP-43 pathology was assessed according to the current criteria (Josephs et al., 2016). One case had TDP-43 pathology present in the subiculum reaching stage 2, two cases contained TDP-43 pathology in the amygdala (stage 1) and the remaining cases were negative for TDP-43 pathology. No TDP-43 or α-synuclein pathology was identified in the control cases used in this study. The demographic data for all cases are shown in Table A.1.

2.3. Amyloid probe staining and imaging

Tissue samples were deparaffinized and rehydrated using xylene and an ethanol:water series followed by equilibration in distilled water. Sections were mounted in 50% glycerol 0.1 M Na_2CO_3 buffer pH 9.5 containing 20 μM K114 and 30 μM CRANAD-3 (structures shown in Fig. 1). Due to the differences in their chemical structure, we reasoned that these dyes would have different affinities and mechanisms of binding to β sheet-rich protein aggregates. K114 emission spectrum occupying the 400–550 nm range with 405 nm excitation and CRANAD-3 covering 550–700 nm range with 488 nm excitation also allowed for good separation of fluorescence originating from either fluorophore. Slides were coverslipped and sealed with UV-curable Bondic liquid plastic sealant to avoid evaporation. The samples were imaged after two-day incubation in the mounting medium containing amyloid dyes. Spectral imaging was performed on an upright Nikon A1R confocal microscope equipped with a 32-channel multianode spectral detector and a 25×, 1.1 NA water dipping objective (Nikon, Japan). Images were
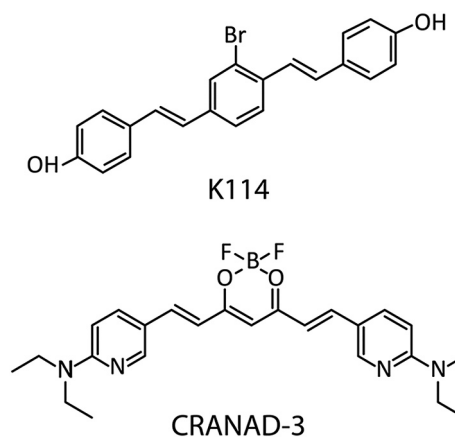

Fig. 1. Chemical structures of K114 and CRANAD-3.

acquired using NIS Elements software version 4.30 with 405 nm excitation, and the spectral detector configured to collect emission ranging from 400 to 720 nm in 10 nm steps. Imaging fields were exposed to 10 passes of high-intensity laser excitation (300 μW measured at the sample at 405 nm) to induce photoconversion of protein aggregates and enhance staining contrast (example in Fig. A.1) (Stepanchuk et al., 2021). CRANAD-3 was imaged using 488 nm excitation and the spectral detector set to collect emission from 495 to 750 nm in 10 nm steps.

2.4. Immunohistochemistry

Amyloid probe staining and imaging were always performed prior to immunohistochemistry because certain steps associated with the latter method (e.g. antigen retrieval) disturb the protein aggregation states on which amyloid dye staining depends. Coverslips of slides previously stained and imaged with amyloid probes were removed and the slides were immersed in distilled water for 5 min to wash off the residual mounting medium. For antigen retrieval, sections were incubated in 95–97% formic acid for 5 min at room temperature and washed in distilled water. Sections were then incubated in blocking solution containing 10% normal goat serum, 1% bovine serum albumin and 0.3% Triton X-100 for 1 h at room temperature. After blocking, the samples were incubated with primary antibodies (mouse anti-amyloid β 6E10, 1:1000 dilution, rabbit anti-tau K9JA, 1:500 dilution in PBS) for 15–17 h at 4 °C. Following three washes (15 min each) with PBS-T (0.05% Tween-20), the slides were incubated with secondary antibodies (Alexa Fluor 488 goat anti-mouse and Alexa Fluor 594 donkey anti-rabbit, 1:500 dilution in PBS) for 1 h at room temperature. After three 15-min washes with PBS-T, slides were mounted in Fluoromount, left for 1 h to cure and imaged on the Nikon A1R confocal microscope. Anti-amyloid β staining with Alexa Fluor 488 conjugated secondary antibody was imaged using 488 nm excitation and spectral detector set up for collection of emission from 495 to 750 nm. Anti-tau staining with Alexa Fluor 594 conjugated secondary antibody was imaged with the 561 nm laser and spectral detector collected emission from 575 to 750 nm.

2.5. Spectral unmixing and analysis of images

At least six separate fields of view were imaged for each slide. Spectral micrographs representing K114 staining, CRANAD-3 staining and both antibodies for immunohistochemistry were acquired for each field of view. Subsequent image processing and analysis were performed using custom-written software (ImageTrak; written by P.K.S. http://stysneurolab.org/imagetrak/).

2.5.1. K114 analysis
Mean emission spectra of amyloid plaques and tau tangles were derived from all images across the AD samples (example in Fig. 4C). Based on our observation that aggregates with a tangle-like morphology exhibited peak K114 emission at 450 nm vs. 520 nm for amyloid plaques, emission spectra with peak maxima at 450 nm and 520 nm were used for linear unmixing and separation of tangle- and plaque-like features from the background parenchyma respectively. The pixels in each image were separated based on the similarity of their emission to background or either of the plaque or tangle spectra.

2.5.2. CRANAD-3 analysis
Average emission spectrum of CRANAD-3 bound to putative diffuse plaques (peak emission at 630 nm, see Fig. 8J) was extracted from images of AD samples. Pixels with predominantly red-shifted CRANAD-3 spectrum were unmixed from the background using the same linear unmixing algorithm as for K114.

2.5.3. Immunohistochemistry
Spectral images of antibody staining were assessed for the presence

of emission spectra characteristic of Alexa Fluor 488 and Alexa Fluor 594. As described above, the features of the image were separated based on the similarity of their emission to background or either of the antibody spectra using linear unmixing (Fig. 2).

2.5.4. Spectral analysis of K114 fluorescence
Variability of emission spectra of K114 bound to amyloid plaques allowed for quantitative spectral analysis of these images (Fig. 3). A band ratio was calculated by dividing integrated emission intensity over the 500–720 nm range by the 400–500 nm intensity band (i.e. a 500 nm split point, Fig. 3D). Based on the band ratio for each pixel, pseudo-colored images were generated, emphasizing subtle changes in emission spectra at different locations of the image, including the differences of plaque emission spectra. The features were colour-coded from violet (low band ratio values, blue-shifted emission spectrum) to red (high band ratio values, red-shifted emission).

For quantitative analysis images were subdivided into kernels, consisting of 3×3 pixels to improve the signal-to-noise ratio. Spectral Scatter Analysis (SSA) plots were generated using fluorescence intensity (Y axis) and band ratio (X axis) for each kernel (Fig. 3C). Each plot was normalized by dividing the intensity value of each kernel by the most frequent intensity value in the image. Such dynamic normalization corrected for the absolute intensity variability across different sections and subregions. The kernels were displayed as a 2D histogram, whereby the more frequent kernels with more frequent intensity/band ratio were coded in warmer colors. Thus, the main cluster of kernels colour-coded in red on each plot represented the background parenchyma, that occupied the majority of the pixels in the image. The presence of high-intensity clusters of kernels on the resulting SSA graphs reflected K114 emission signatures associated with different protein aggregates (Aβ plaques and tau tangles). Quantitative analysis of CRANAD-3 images was performed in a similar manner using a 595 nm split point for the band ratio and red-shifted kernels were selected for quantification of diffuse amyloid deposition.

Weighted scores were calculated by selecting the same region of interest (ROI) across all SSA graphs, computing a mean score (=band ratio × intensity), then multiplying by the proportion of kernels within the ROI (Stepanchuk et al., 2020). This correction was necessary to avoid having a small number of rogue kernels resulting in widely ranging score values.

3. Results and discussion

3.1. Aβ and tau deposits can be distinguished by different emission signatures of K114

K114 exhibited two distinct emission signatures when bound to two morphologically different types of protein aggregates (truecolor image shown in Fig. 4A1). The blue-shifted spectrum with peak emission at 450 nm characteristic of spindle-shaped neurofibrillary tangles and the red-shifted signature with peak emission at 520 nm seen in more diffuse amyloid plaques were unmixed into separate channels and compared with immunohistochemistry (Fig. 4A, B). Notably, such spectral unmixing revealed clear presence of tangle-like pathology within the senile plaques,

that is not readily apparent in the truecolor images. Immunostaining of the same section showed significant correlation between 450 nm K114 unmixing results and tau-positive IHC signal, as did 520 nm unmixing with anti-Aβ antibody staining (Fig. 4A, B). Interestingly, there were substantial differences in the labeling intensity of certain K114 and IHC-positive features. For example, immunostaining of some plaque cores was much weaker compared to K114 staining of the same deposits (Fig. 4A3 and B3, arrow). Tau tangles exhibited even more drastic differences between K114 and immunolabeling, whereby some aggregates were detected by both methods and others were not stained with antibodies at all (Fig. 4D, asterisks). This underscores the
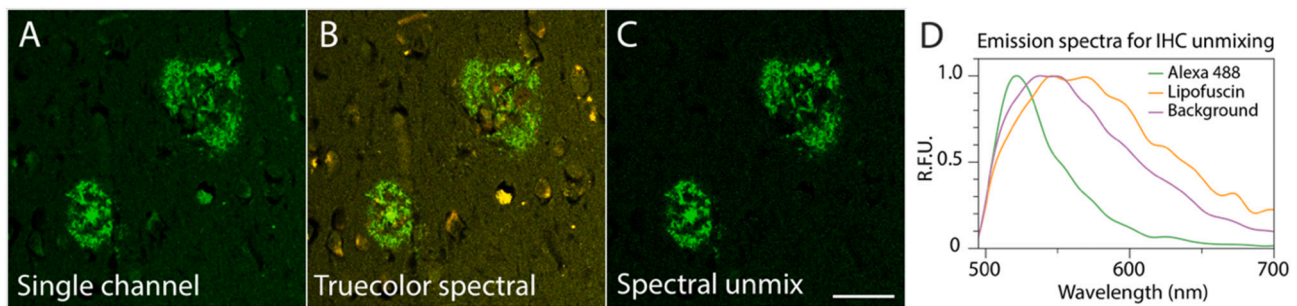
Fig. 2. Spectral imaging and unmixing of human brain samples improves specificity of immunofluorescence staining. Single channel confocal images of Aβ immunostaining (A) were degraded by tissue autofluorescence. Acquisition of spectral images (B) and subsequent unmixing of antibody emission spectra from the autofluorescent brain parenchyma allows for better separation of the antibody signal and prevents unwanted tissue autofluorescence from interfering with specific antibody staining (C: results of unmixing; D: emission spectra recorded from spectral images and used for unmixing). Scale bar: 50 μm.
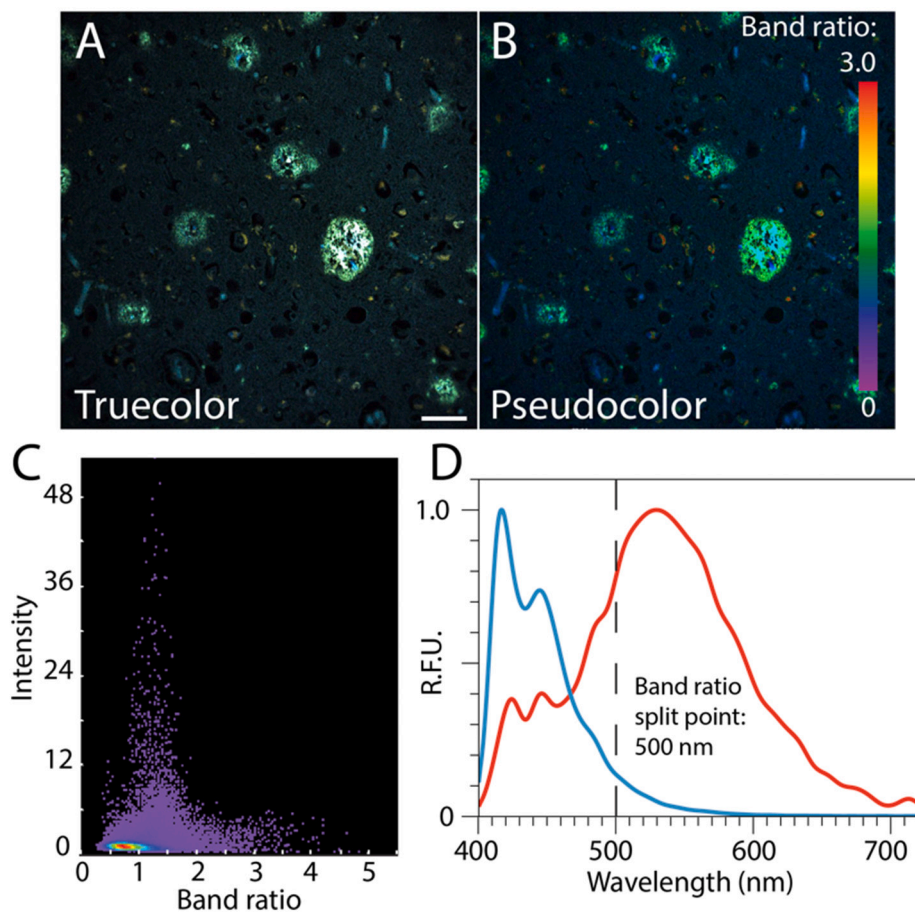

Fig. 3. Example of quantitative spectral analysis of K114-stained human AD brain sections. Based on the band ratio of emission intensities with a 500 nm split point, spectral images (A: truecolor image) can be pseudocolored to enhance subtle changes in emission spectra in various regions, including intraplaque emission differences (B). The same principle is used to calculate Spectral Scatter Analysis (SSA) plots (C) for quantitative image analysis, where each pixel of the image is plotted based on its emission band ratio (X axis) and integrated intensity (Y axis). An example of two different K114 emission spectra from neurofibrillary tangles (blue) and amyloid plaques (red) is shown in D. Scale bar: 50 μm. (For interpretation of the references to colour in this figure legend, the reader is referred to the web version of this article.)

complementarity of the two methods: K114 reports aggregates of misfolded amyloids (both Aβ and tau, yielding different emission spectra), whereas antibody staining will be agnostic to the misfolding state of its cognate protein, reporting only the density of the deposit with no spectral shift from the fluorescent secondary antibody. Moreover, being a small organic molecule, K114 will be better able to access tight amyloid binding pockets and emit bright fluorescence, whereas these sites may be inaccessible to much larger IgG molecules even after antigen retrieval, leading to an underestimate of high-density amyloid deposits. Taken together, the propensity of K114 to label β-sheet-rich amyloids, rather than proteins independent of their folding states, together with robust spectral shifts, allows quantitative and unbiased estimates of disease-relevant amyloid accumulation in tissue sections as illustrated in

the next section.

3.2. Quantitative assessment of Aβ and tau pathology using K114 and Spectral Scatter Analysis

Spectral micrographs are very information-rich, containing large variations in emission wavelengths and intensities. However, unlike 2 or 3 channel fluorescence images where simply comparing intensities and co-localizing various labels, objective analysis of spectral images can be challenging. We addressed this problem by assigning an intensity and spectral shape (reflected by band ratio, see Methods) to each pixel, then plotting these numerical pairs on a Spectral Scatter Analysis (SSA) graph. Fig. 5A1 shows a spectral micrograph of a human amyloid plaque
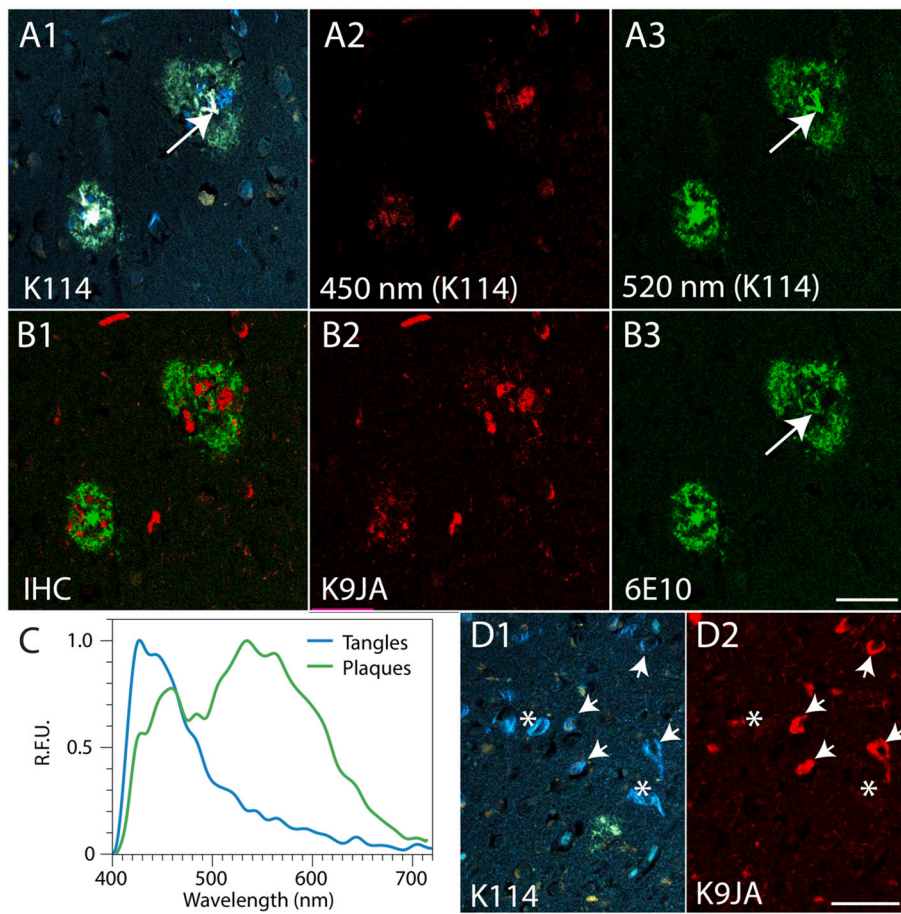
Fig. 4. Different emission spectra of K114 can be attributed to morphologically and biochemically distinct protein aggregates. Staining a neuropathologically-confirmed section of AD brain with K114 revealed, within a single spectral image, a more complete picture of misfolded protein deposition compared to immunohistochemistry. Two emission colors associated with morphologically different aggregates (green senile amyloid plaques and blue neurofibrillary tangles) are visible in the truecolor image (A1), with corresponding spectra in (C). Their distinctiveness allowed a reliable unmixing of the two emissions into separate channels as shown in A2 and A3. Immunohistochemistry confirmed the protein composition of the two deposits with Aβ-rich plaques (6E10, green) and tau-rich tangles (K9JA, red) (B1–B3). Of interest is that K114 signal and IHC staining were often but not always concordant, e.g., V-shaped deposit marked with arrows across the panels within the plaque core in A1 was strongly labeled by K114, exhibiting a spectrum consistent with Aβ (A3), whereas this feature exhibited relatively weak immunolabeling with 6E10 (B3); similarly, not all tangles were labeled equally with K114 and the anti-tau antibody K9JA: tangles that were detected by both methods - arrows; tangles that were not detected by IHC – asterisks (D1, D2). Scale bars: 50 μm. (For interpretation of the references to colour in this figure legend, the reader is referred to the web version of this article.)

stained with K114, which appears bright green against a dark background. The corresponding SSA is shown in Fig. 5B1, with pixel intensities plotted along the Y-axis, and band ratios along the X-axis, with more red-shifted spectra assuming higher band ratios. The SSA represents in effect a 2D histogram with the most frequent pixels colored in red. The main red cluster at the bottom left of the graph therefore represents the majority of dim background pixels, while pixels originating from the plaques occupy a very distinctive position on the SSA being at the same time much more intense, and spectrally red-shifted compared to the weak background fluorescence. An ROI can be drawn to select this plaque cluster, with the corresponding pixels in the original image enclosed by this ROI shown by the green mask in C1. Quantitative analysis can now be performed on the selected plaque pixels. For instance, these pixels represent 9.9% of the total, which can be an estimate of plaque density; their mean index is 2.08 compared to 0.79 for the background indicating a distinctly different red-shifted spectrum, and a mean normalized intensity of 5.7 indicating that this feature is ≈5 fold brighter in relative terms than the background.

The above example was deliberately selected as a simple image containing mainly dim background and spectrally homogeneous plaques. The SSA method is very well suited for analysis of more complex spectral micrographs. Fig. 5A2 shows an example of a human AD brain section containing both plaques and tangles. As shown in Fig. 4 these deposits exhibit very distinct emission spectra when stained with K114 under our conditions, with tangles being bluer (yielding lower band ratios) vs. amyloid plaques exhibiting longer wavelength fluorescence (higher band ratios). In addition to the dim main background cluster, the corresponding SSA (Fig. 5B2) now shows two distinct high-intensity populations representing the tangles (blue ROI) and plaques (green ROI), and confirmed by the masks in 5C2. Quantitation showed that the

plaque pixels had a mean index of 1.31 ± 0.18 and comprised 4.6% of total pixels, while the tangles had a mean index of 0.39 ± 0.01 and occupied 2.5% of the total area.

While the colour differences between plaques and tangles are visually obvious, we also observed spectral variations *within* a single plaque. These shifts were more subtle so that visually all plaques appeared uniformly green (Fig. 5A1–3). However, quantitative SSA analysis revealed significant spectral variation even within the same plaque, as shown in the example in Fig. 5A3–C3. In contrast to the plaques in 5A1 and 5A2, the plaques in 5A3 exhibited much larger spectral variation as shown by the spread of points along the X-axis in Fig. 5B3, with a mean of 1.5, but with a considerable variance spanning a range of 0.6 to 2.5 (SD: 0.35). Here the large plaque exhibited a core that had lower band ratio values (blue-shifted fluorescence) likely corresponding to tighter more hydrophobic amyloid assemblies (Stepanchuk et al., 2021) compared to the rim that emitted at longer wavelengths. The continuous distribution of points along the X axis in 5B3 confirms a continuous spectral spread in the plaque, and therefore likely a continuum of amyloid assemblies. These findings underscore the major advantage of our approach compared to conventional immunostaining: not only can K114 labeling distinguish deposits formed by different proteins, but it can also reveal fundamentally different structural assemblies made of the same protein, such as the vascular and parenchymal amyloid in 6A1-C1, or compact vs. more diffuse amyloid within the same plaque in Fig. 5C3.

3.3. K114 exhibits significant spectral variability when bound to different types of amyloid deposits

In Alzheimer's brain, Aβ not only appears as distinct extracellular deposits in the parenchyma in the form of senile plaques, but also
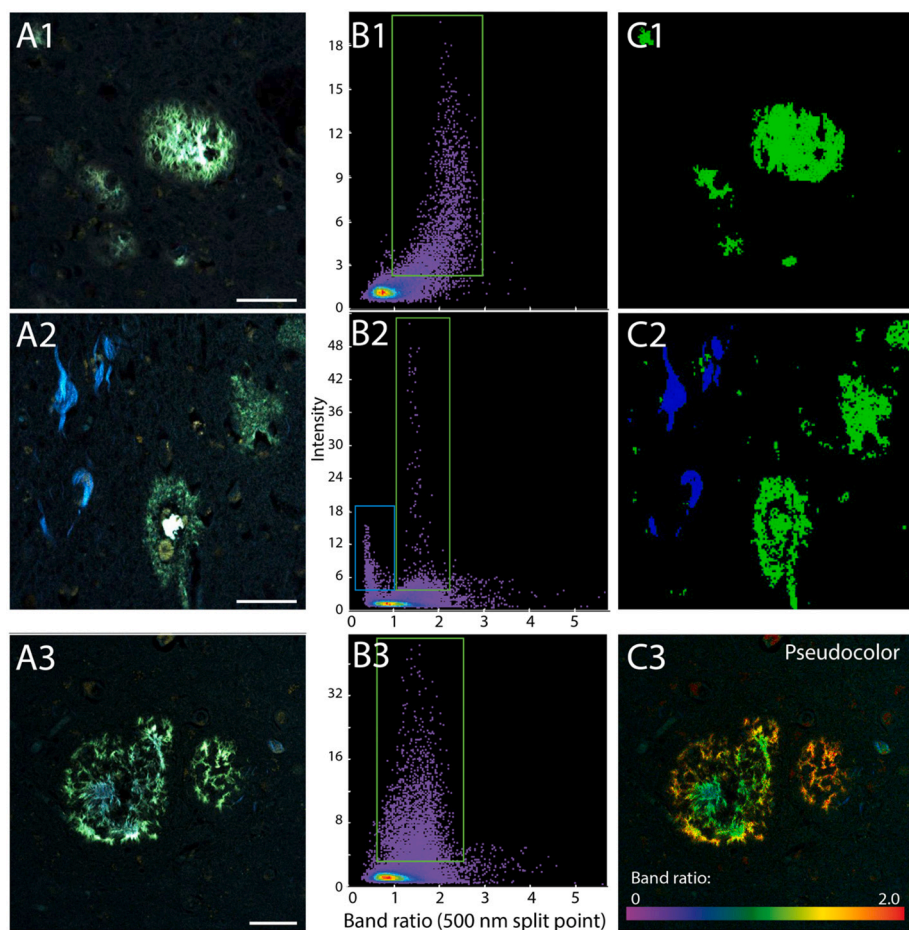
Fig. 5. Band Ratio Spectral Scatter Analysis of K114-stained AD samples. Representative truecolor spectral images of human AD plaques and tangles are shown in panels A1–A3. Quantitative analysis of plaque and tangle deposition was performed by plotting pixels from each image based on their band ratio (X axis) and intensity (Y axis) on SSA graphs (B1–B3). When bound to protein deposits, K114 exhibited a significant increase in fluorescence intensity, which was reflected by the presence of high intensity kernels in all three graphs enclosed by the ROIs. Selection of the high-intensity red-shifted cluster in B1 (green ROI) selected the pixels corresponding to the plaque in the original image (C1). Two different types of aggregates (blue tangles and bright green plaques, A2) are reflected in the SSA graph as two separate high intensity clusters located at different band ratios along the X axis (B2). These clusters (blue and green ROIs) correspond to respective tangle- and plaque-like features in the original image (C2). Band ratio can be also used for pseudocoloring for visual emphasis of the subtle differences in tissue emission spectra even within a single deposit. A truecolor image that hints at intraplaque spectral differences (A3), clearly shows the heterogeneity of emission signatures both on the SSA graph (B3) and the pseudocolored rendition (C3). Scale bars: 50 μm. (For interpretation of the references to colour in this figure legend, the reader is referred to the web version of this article.)

frequently accumulates in the walls of blood vessels resulting in cerebral amyloid angiopathy (CAA). Moreover, plaques are enriched in aggregated Aβ(1–42) peptide, whereas in vascular amyloid the shorter cleavage product Aβ(1–40) predominates (Gravina et al., 1995; Serrano-Pozo et al., 2011; Greenberg et al., 2020). Given the different peptide constituents, it is likely that the resulting amyloid assemblies might differ at the nanostructural level. We explored whether K114 spectroscopy could distinguish between these two amyloid types, as well as revealing different spectral characteristics of various plaques (also see the comparison of CAA autofluorescence with normal vessel fluorescence and K114 staining in Fig. A.2). Fig. 6 shows examples of an amyloid plaque together with an amyloid-laden blood vessel (top row), and dense core plaques exhibiting different spectral character (bottom row). Column A indicates that all these amyloid deposits were enriched in Aβ as evidenced by robust immunolabeling with 6E10. K114 truecolor images (column B) hint at some variability in hue, with the vascular amyloid appearing bluer than the plaque (B1), and the two large plaques exhibiting different hues in B2. The pseudocolor images in column C confirm the different emission spectra, quantitatively plotted in the corresponding SSA graphs (column D). Two distinct clusters are seen in D1 corresponding to the blue-shifted vascular amyloid and a redder emission from the plaque. D2 also shows two distinct clusters corresponding to the two plaques which clearly exhibit spectrally distinct amyloid accumulation. Note that the bluer plaque (#4) has a similar emission to the plaque in B1 (#1), and plaque #3 in B2 has a much redder spectrum with band ratios approaching 3. Importantly however, although plaques exhibited significant intra- (Fig. 5A3–C3) and inter- (Fig. 6A2–D2) plaque variability, vascular amyloid tended to emit with the shortest wavelength fluorescence strongly supporting the idea of fundamentally different amyloid assemblies in these structures, that

could be driven by a different aggregation mechanism.

3.4. Quantification of pathological protein deposition across cases using Spectral Scatter Analysis

While plaque pathology characteristically involves cortical regions in AD, there are also reports of white matter amyloid deposition in this disease (Collins-Praino et al., 2014; Iwamoto et al., 1997). We applied the SSA method to analyze gray and white matter regions from 6 control and 6 AD cases confirmed by standard neuropathological examination (Table A.1). Representative K114-stained spectral micrographs of control vs AD cortex, and subcortical white matter, are shown in Fig. 7D–G. For this analysis, cortical regions and subcortical white matter from the anterior cingulate, hippocampus and temporal cortex were used. Fig. 7A1–B2 shows aggregate SSAs, combined from all control and AD gray and white matter regions. ROIs were drawn to select plaque-like structures in both gray and white matter. In the control gray matter group, a few high-intensity clusters (Fig. 7A1, arrows) were seen corresponding to infrequent amyloid plaques found in otherwise healthy older brains (Rodrigue et al., 2009; Armstrong et al., 1996; Dickson et al., 1992). Notably, this cluster was much less heterogeneous compared to the amyloid plaque signal in the gray matter AD SSA, which was far more prevalent in the AD cases (0.04% of total kernels in control vs. 0.2% of total kernels in AD, $p = 0.002$, Wilcoxon signed-rank test) showing higher intensities and a much broader spectral range (Fig. 7B1). Because plaques exhibited both higher intensities and red-shifted spectra (higher band ratios), in order to capture both features we calculated a score which was the product of intensity and band ratio for each point, which will capture both an increase in intensity and a red-shift of the spectrum. Mean scores were weighted by frequency as
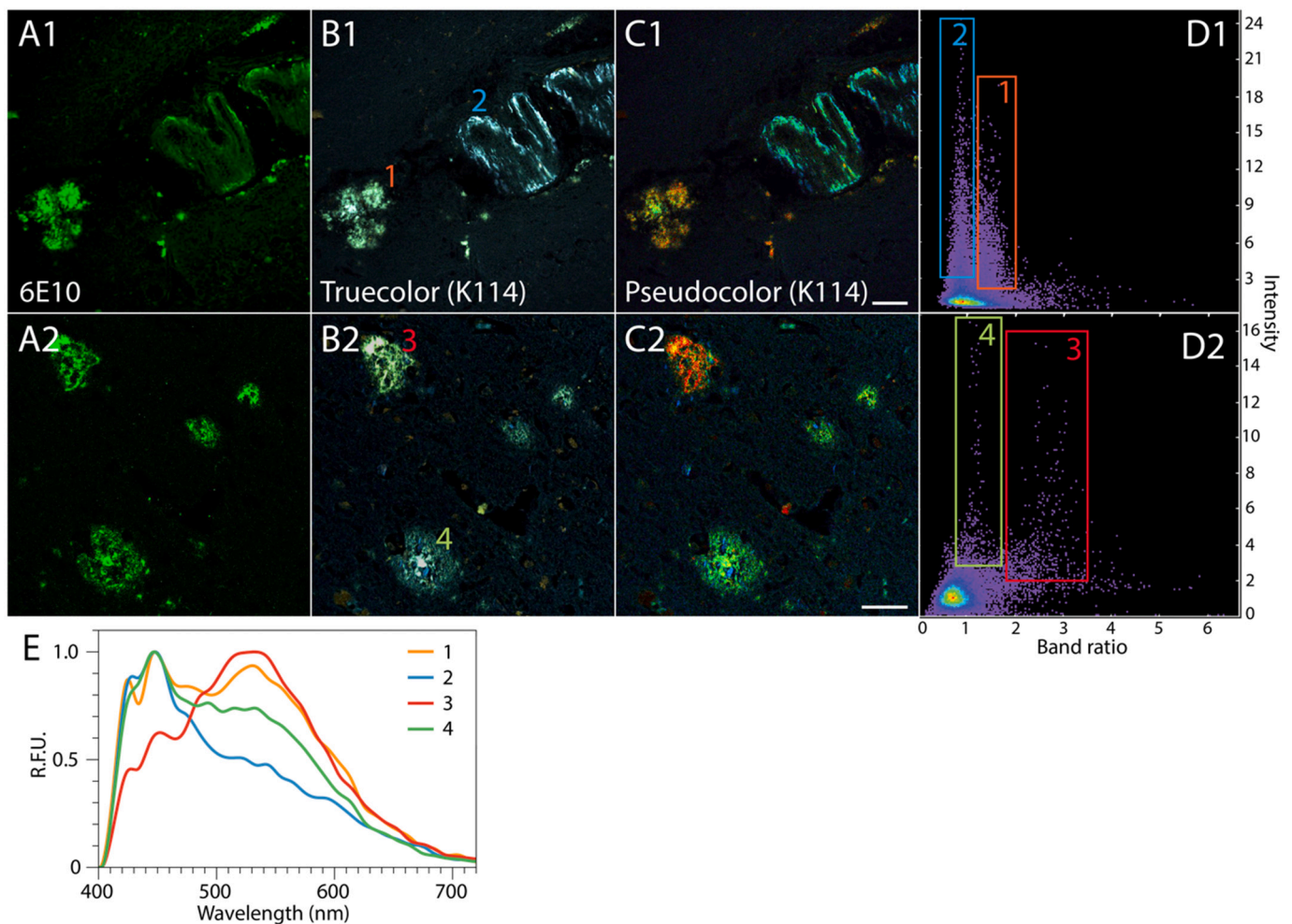
Fig. 6. Spectral analysis of various Aβ deposits in AD brain sections. Examination of K114-stained Alzheimer's samples reveals a variety of emission signatures associated with different types of amyloid deposits. For example, 6E10-positive (A1) vascular amyloid and amyloid plaque appear to have different colors in the K114 truecolor image (B1, parenchymal amyloid plaque – #1, vascular amyloid – #2), which is further enhanced using band ratio pseudocoloring (C1). Vascular amyloid had a blue-shifted emission spectrum compared to the plaque, which is reflected in the corresponding SSA graph as two distinct clusters of high-intensity kernels: one with band ratios from ~0.3–1.0 representing deposits in the vessels and a cluster spanning 1.2–2.0 from the amyloid plaque (D1, blue and orange ROIs). Significant variation of emission signatures can also be seen in different amyloid plaques located in the same tissue section. Despite roughly similar morphological appearance (A2), these plaques exhibit different colors when stained with K114 (B2) and this difference is further enhanced in the pseudocolored image (C2). Two clusters enclosed by green and red ROIs on the SSA graph (D2) correspond to the plaques in A2-C2. Scale bars: 50 μm. (For interpretation of the references to colour in this figure legend, the reader is referred to the web version of this article.)

explained in Methods, to mitigate effects of infrequent outliers. Mean weighted scores for each of the 6 controls and 6 AD cases are plotted in Fig. 7C1&2, confirming in a quantitative manner the large excess of amyloid pathology in the AD cases. A similar analysis of white matter regions also revealed significant amyloid pathology (large neocortical plaques in the immediate subcortical white matter) in AD vs controls ($p = 0.002$, Wilcoxon signed-rank test for both gray and white matter weighted scores, Fig. 7C2).

An unexpected and striking observation was the marked difference in spectral variance between age-related vs AD-associated amyloid deposits. Variances (rather than mean band ratios) are plotted for gray and white matter regions in Fig. 7H, with the AD samples showing much greater heterogeneity (p = 0.002 for gray and white matter, Wilcoxon signed-rank test). This suggests that age-related plaques might be driven by a different process, resulting in not only less amyloid accumulation, but also a more homogeneous type of amyloid deposition compared to AD, whereas AD might have a mix of age- and disease-related pathology. Alternatively, different plaque morphologies could represent distinct plaque maturation stages, with the diffuse plaques forming at the earliest point, and the more complex and heterogeneous plaques

occurring stochastically over time due to multiple mechanisms. The pathophysiological implications for neurodegeneration and clinical deficits are unclear at this time, but this raises the intriguing possibility that different varieties of amyloids, driven by different biological processes, could underlie benign normal aging vs. more pathological disease states, with K114 spectroscopy having the ability to distinguish between the two.

3.5. K114 and CRANAD-3 revealed different aspects of amyloid pathology in 5xFAD brain

As illustrated above, K114, like a number of other fluorescent amyloid probes (Levine, 2005; Styren et al., 2000; Zhang et al., 2018; Crystal et al., 2003; Hammarström et al., 2010) exhibited significant and highly informative spectral shifts when contacting various amyloid deposits. However, it is also known that different dyes stain different protein aggregates with widely varying efficiency (Magnusson et al., 2014; Zhou et al., 2019). We reasoned that combining K114 with a second amyloid dye, selected from a different chemical family than derivatives of Congo Red, and having different excitation/emission spectra, could provide
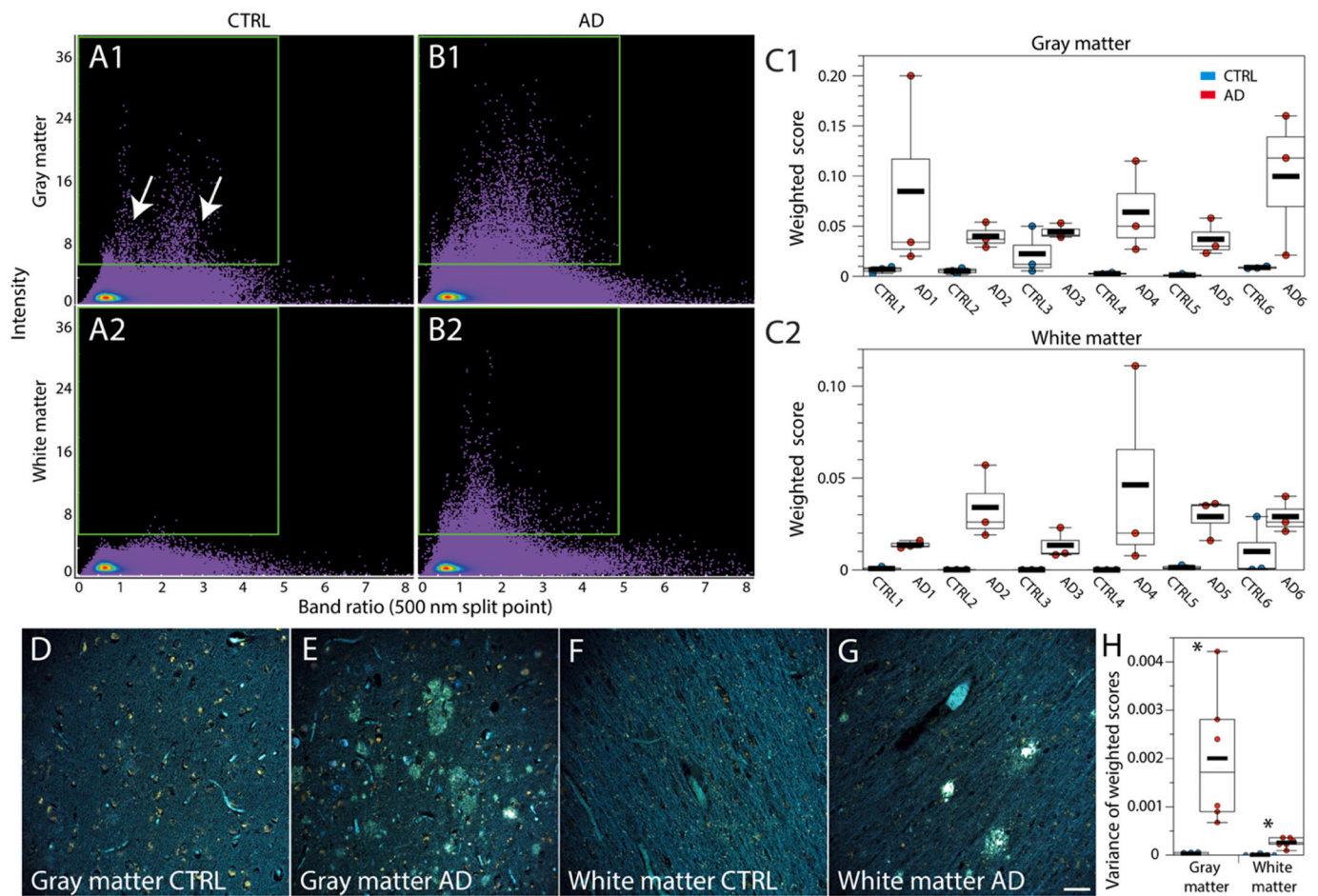
Fig. 7. Quantitation of protein aggregation in control and AD cases using Spectral Scatter Analysis on K114-stained brain sections. A1-B2 are pooled SSAs from gray and white matter regions, from all control and AD cases for overall comparison. The same region of interest (green rectangle) was applied to the four plots to enclose higher-intensity kernels that excluded the background parenchyma. Such high intensity kernels, occasionally seen in gray matter of control cases (A1, arrows; 0.04% of total kernels) were much more abundant and variable in the pooled AD gray matter SSA (B1; 0.2% of total kernels). While white matter of control cases was practically devoid of bright aggregates (A2), the AD SSA reflected a significantly higher load of subcortical white matter amyloid pathology (B2). The kernels enclosed within the ROIs were then quantified for both gray and white matter for each case separately. The weighted scores of three brain regions (anterior cingulate, temporal cortex and hippocampus, each represented by a separate dot) are shown for each case in panels C1 and C2 for gray and white matter images respectively. The variance of weighted scores across the cases was highest for AD gray matter (H, $p = 0.002$, Wilcoxon signed-rank test). Representative images of gray and white matter of control and AD cases are shown in panels D-G. Scale bar: 50 μm. (For interpretation of the references to colour in this figure legend, the reader is referred to the web version of this article.)

additional information about misfolded protein aggregation in tissues. We chose CRANAD-3, an analog of curcumin having excitation and emission spectra that are red-shifted by ≈100 nm compared to K114, as a complementary reporter. Examples of 5xFAD mouse brains of various ages, double-stained with both K114 and CRANAD-3, are shown in Fig. 8, together with whole brain images in Fig. A.3.

Staining of 5xFAD brain sections with K114 (A,C,E,G) showed an increase in plaque burden with age, typical for this strain (also see Fig. A.3 for whole brain overviews). The spectral signatures of K114 fluorescence associated with amyloid plaque deposits became slightly more red-shifted with age, exhibiting a characteristic broad peak at ≈550 nm (Fig. 8I) (Levine, 2005; Stepanchuk et al., 2021; Crystal et al., 2003). Co-staining of the same sections with CRANAD-3 (B, D, F, H) revealed a very different pattern compared to K114. At younger ages, plaque cores were only weakly labeled by CRANAD-3 compared to K114. In contrast, CRANAD-3 reported prominent red-shifted diffuse plaque rims surrounding K114-positive amyloid cores, first appearing in 6 month-old samples (D) and increasing with age. These satellite deposits were far more extensive by CRANAD-3 fluorescence compared to K114. Neither of the two distinct signatures of CRANAD-3, whenever present, changed with age. The mean emission spectra of K114 and

CRANAD-3 associated with different features are shown in Fig. 8I and J respectively. Interestingly, while K114 exhibited a single albeit variable emission peak associated with 5xFAD plaques, CRANAD-3 revealed two distinct emission spectra when bound to amyloid deposits: a relatively blue-shifted spectrum with a main peak in the 525–550 nm range, originating from plaque cores, and a much redder emission (≈630 nm peak) from plaque rims. The differences in the excitation wavelengths of the two dyes as well as their ability to label distinct types of amyloid aggregates allowed us to use K114 and CRANAD-3 simultaneously for staining human brain samples without the ambiguity of fluorescence overlap, as shown in the next section.

3.6. CRANAD-3 complements K114 by detecting diffuse Aβ deposits in human AD samples

Having confirmed that K114 and CRANAD-3 label different types of Aβ deposits in 5xFAD mouse brain sections, we used the same staining approach on human tissue. In the example shown in Fig. 9, the images acquired using 488 nm (CRANAD-3) and 405 nm (K114) excitation were strikingly different. Panel 9A1 shows a truecolor image of a human AD brain sample stained with CRANAD-3 and excited at 488 nm. Notably,
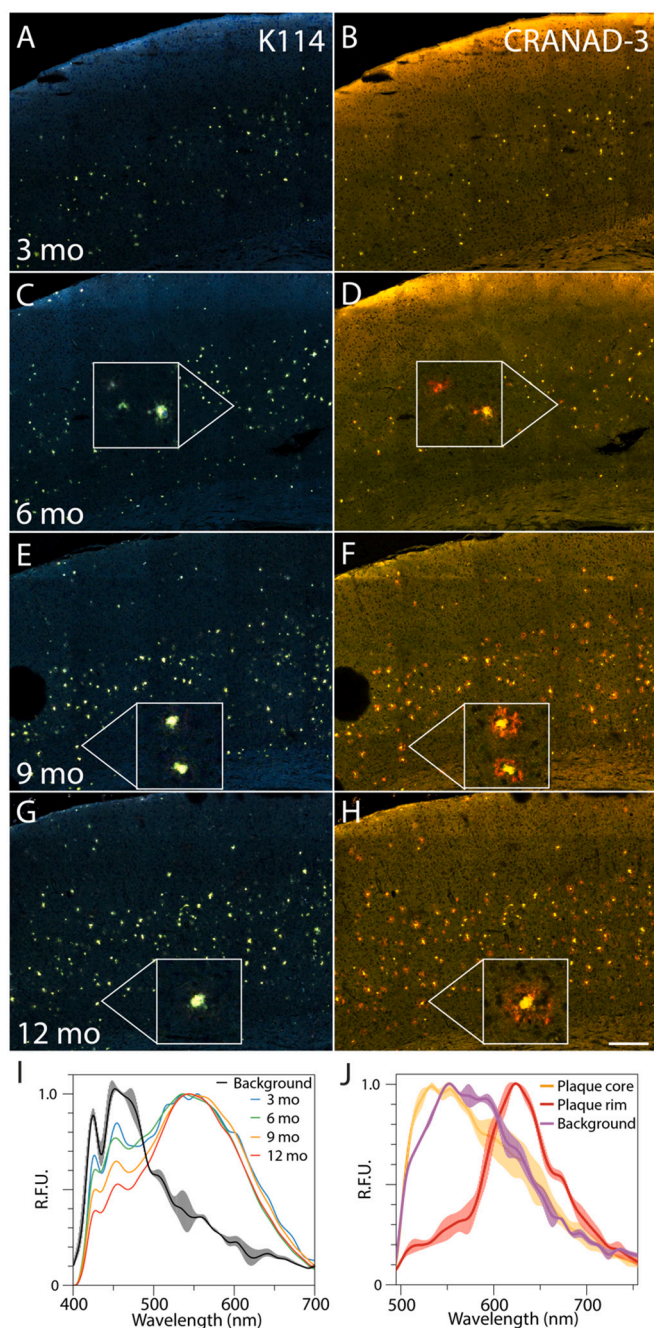
Fig. 8. K114 and CRANAD-3 are complementary in their reporting of different types of amyloid deposits in 5xFAD mouse brain sections. Increase of plaque burden with age is characteristic of the 5xFAD mouse model of AD. Comparing 3, 6, 9 and 12-month-old brain sections shows that both K114 (A, C, E, G) and CRANAD-3 (B, D, F, H) detected this progression of amyloid pathology. Starting from 6 months of age, CRANAD-3-stained diffuse aggregates surrounding plaque cores that were not labeled by K114. The abundance of these red-shifted deposits increased in older mice. I - average emission spectra of K114 in background tissue parenchyma and amyloid plaques across different ages. J – average emission spectra of CRANAD-3 in background parenchyma, plaque cores across all ages and plaque rims (6 months and older). Error bars in I and J are SEM. Scale bar: 200 μm. (For interpretation of the references to colour in this figure legend, the reader is referred to the web version of this article.)

this wavelength also excites fluorophores inherently present in the tissue, such as lipofuscin, often leading to autofluorescence bleed-through and false-positive contribution to the detected signal in conventional four-channel confocal microscopy. As a result, in addition to the two main plaque types labeled by CRANAD-3 (asterisk and arrow), the image also contains numerous bright yellow lipofuscin granules. The differences in emission spectra of lipofuscin and CRANAD-3 bound to both dense core plaques (asterisk, 530 nm peak) and diffuse red-shifted deposits (arrow, 630 nm peak) allowed for the separation of amyloid-related signal from unwanted tissue autofluorescence using spectral unmixing (Fig. 9A2). Interestingly, CRANAD-3 emission signatures in human AD plaques were similar to the spectra in 5xFAD deposits (Fig. 8J).

Compared to 488 nm that strongly excites lipofuscin (among other autofluorescent species), 405 nm predominantly excites NAD(P)H and flavins. K114 signal produced by 405 nm excitation was much less contaminated by autofluorescence from the latter species, the contribution of which was also minimized due to overall brightness of this dye (Fig. 9B1). Interestingly, although mature plaques (marked with an asterisk at the bottom of the field of view) were labeled very strongly, the red diffuse plaque (arrow), that was robustly detected by CRANAD-3, was not labeled by K114 at all, which was further confirmed by spectral unmixing shown in Fig. 9B2. An overlay of the unmixing results from both dyes underscores the complementarity of the dual probe approach (Fig. 9C). Neither of the dyes *alone* matched the sensitivity of IHC (Fig. 9D), however, co-staining of the sample with both K114 and CRANAD-3 not only surpassed the sensitivity of the Aβ immunolabeling, but also provided valuable information about conformation, which antibody labeling was unable to provide.

We found that human samples exhibited much less dense core amyloid with 530 nm CRANAD-3 maximum emission peak than mice. In contrast, human AD cases had more red-shifted diffuse deposits that were present predominantly as separate clusters in the parenchyma, not in close proximity to the dense yellow cores, nor to K114-positive mature amyloid plaques. This observation provides further evidence for different underlying mechanisms of Aβ aggregation in the 5xFAD mouse model compared to human sporadic AD. Quantitative analysis using SSA of CRANAD-3 staining across all human samples is shown in Fig. A.4.

3.7. CRANAD-3 does not stain K114-positive neurofibrillary tangles

We showed above that CRANAD-3 could detect diffuse K114-negative Aβ aggregates and the cores of some mature plaques. As shown in Fig. 10, abundant K114 signal in both plaque- (arrows) and tangle-like (asterisks) features, overlapped with the immunolabels (K114 truecolor image shown in 10A, Aβ IHC – 10C, tau IHC – 10D). In contrast, CRANAD-3 showed no affinity towards any of the above-mentioned deposits in this sample (Fig. 10B). No neurofibrillary tangle staining by CRANAD-3 was detected in any of the cases in this study. Different affinity of K114 and CRANAD-3 towards various misfolded protein deposits in AD samples – with tangles a particularly notable example – supports the complementary nature of the dual probe staining approach.

4. Discussion

Protein aggregation in Alzheimer's disease brain can exhibit variable patterns, including differential deposition of the characteristic extracellular Aβ-rich amyloid plaques and intraneuronal neurofibrillary tangles composed of hyperphosphorylated and aggregated tau filaments (Arnold et al., 1991; Braak and Braak, 1991). This deposition is not random, but follows a stereotyped anatomical progression with amyloid plaque accumulation beginning in the neocortex, and tangles first appearing in the entorhinal cortex (Thal et al., 2002). Interestingly, recent evidence suggests that heterogeneity exists not only at the anatomical level, but also at the molecular level, with evidence of a number of Aβ strains or "morphotypes", akin to the better known strain variability of prion protein conformers (Condello et al., 2018; Watts et al., 2014; Cohen et al., 2016). Using conformation-dependent
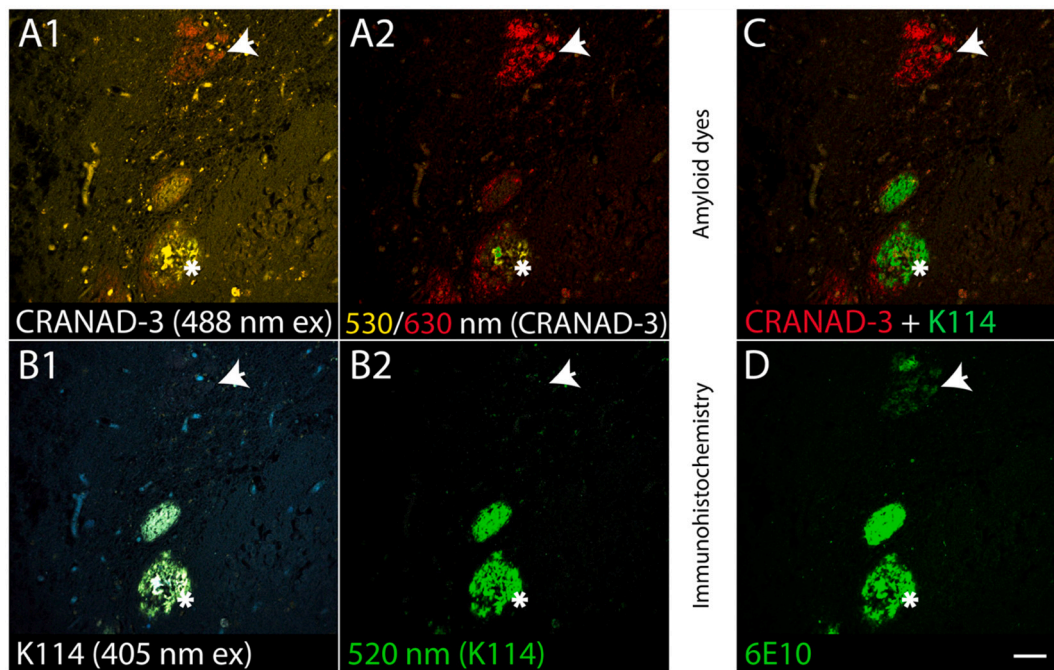
Fig. 9. Comparison of dual amyloid probe staining with immunofluorescence of Alzheimer's plaques. This sample was notable for abundant diffuse plaques with fewer dense core plaques. CRANAD-3 (A1: truecolor image, A2: unmixed 530 nm and 630 nm peaks) revealed distinct diffuse orange deposits (arrow) indicative of diffuse senile plaques, as well as the yellow centers of the dense-core plaques (asterisk). In contrast, K114 preferentially reported the dense-core plaques, showing no labeling of the diffuse plaque (arrow in B1) (B1: truecolor image, B2: unmixed 520 nm peak). The overlay of K114 and CRANAD-3 unmixing results is shown in C. The diffuse deposits were mainly red corresponding to CRANAD-3 signal, whereas dense core and more mature plaques were mainly green, reported by K114, with a significant overlap of the 530 nm CRANAD-3 peak and K114 520 nm peak revealing that both probes were able to bind to these species. Overlaying both dyes shows their complementary reporting abilities with respect to plaques, confirmed by 6E10 immunostaining (D). Scale bar: 50 μm.

immunoassay, Cohen and colleagues reported that differences in Aβ (1–42) conformation may underlie differences in the rate of Alzheimer's progression (Cohen et al., 2015). Moreover, it has been proposed that such plasticity of Aβ and tau conformers might underlie different clinical disease phenotypes, such as predominantly amnestic syndromes, posterior cerebral atrophy affecting visuospatial function, logopenic presentations (language dysfunction) and frontal lobe syndromes (personality changes, apathy) (Villain and Dubois, 2019; Lam et al., 2013). Taken together, data now strongly suggest that not only spatial heterogeneity of plaque and tangle deposition, but also nanostructural variability of prion-like Aβ and tau strains, both play a role in determining the pathological and clinical phenotypes (Holmes and Diamond, 2014; Lau et al., 2020; Jucker and Walker, 2018; Prusiner, 2012). Established histological methods such as silver staining and immunohistochemistry are well suited for studying the distribution of traditional Alzheimer's pathology at the microscopic level, but are unable to reveal conformational heterogeneity of Aβ and tau aggregates, which is emerging as a potentially important aspect of disease pathogenesis. Elucidating this "nanostructural pathology" is more challenging, requiring sophisticated methods such as conformation-dependent immunoassay, cryo-EM or solid-state NMR spectroscopy (Lau et al., 1777; Shewmaker et al., 2011; Cohen and Calkins, 1959), which do not preserve tissue morphology.

Certain classes of small organic fluorophores are known to exhibit a high affinity for amyloid, and are very useful for detecting such deposits in a variety of neurodegenerative disorders. These dyes have been used for visualization of aggregated β-sheet-rich deposits in brain sections for almost a century (Kollmer et al., 2019). The phenomenon of preferential binding of amyloid fluorophores to the tight hydrophobic pockets in fibrils has been harnessed to develop a variety of probes with unique physicochemical properties (Bennhold, 1922; Nesterov et al., 2005; Verwilst et al., 2018; Reinke and Gestwicki, 2011). The new generation of amyloid probes aims to improve our ability to detect different

amyloid species, including those that are not readily visualized by conventional techniques (e.g., prefibrillar species and oligomers). The key difference that sets labeling with amyloid probes apart from immunohistochemistry is the ability to report and *distinguish* different types of β-sheet-rich protein aggregates, with simultaneous preservation of tissue morphology. Indeed, as illustrated in this report and others (Cao et al., 2018; Chu et al., 2017), amyloid staining can be combined with immunohistochemistry to take advantage of the specificity for detection of different proteins that the latter method offers.

The ability to change the structure of amyloid fluorophores to increase the affinity towards certain aggregates, combined with the very different chemical structures of amyloid probe families, implies that no single molecule would detect all species of misfolded proteins equally well. We took advantage of this heterogeneity of amyloid dye behavior and reasoned that combining two probes from different dye families (K114, a Congo Red derivative; and CRANAD-3, based on curcumin) (Crystal et al., 2003; Brelstaff et al., 2015; Ran and Moore, 2012) would increase our ability to detect a broader range of misfolded protein aggregates reported by spectral variation of the emitted fluorescence. Our data from 5xFAD Alzheimer's mice confirmed this prediction. While K114 alone exhibited very interesting behavior in terms of spectral variation in different amyloid deposits (Figs. 3–7), including the ability to report marked heterogeneity within a single plaque (Fig. 5), we show that co-staining the sections with these two probes revealed a much richer picture of misfolded protein pathology than either dye alone. While K114 stained the cores and the fibrillar threads of the amyloid plaques better than CRANAD-3 at all ages, the curcumin derivative additionally reported diffuse red-shifted plaque rims that started appearing in 6-month-old sections and increased with age; these were not detectable by K114 (Fig. 8). In turn, phospho-tau-rich neurofibrillary tangles were not stained by CRANAD-3, but were brightly labeled by K114 with a characteristic blue-shifted emission spectrum (Figs. 4 and 10), further underscoring the complementarity of these two dyes and the
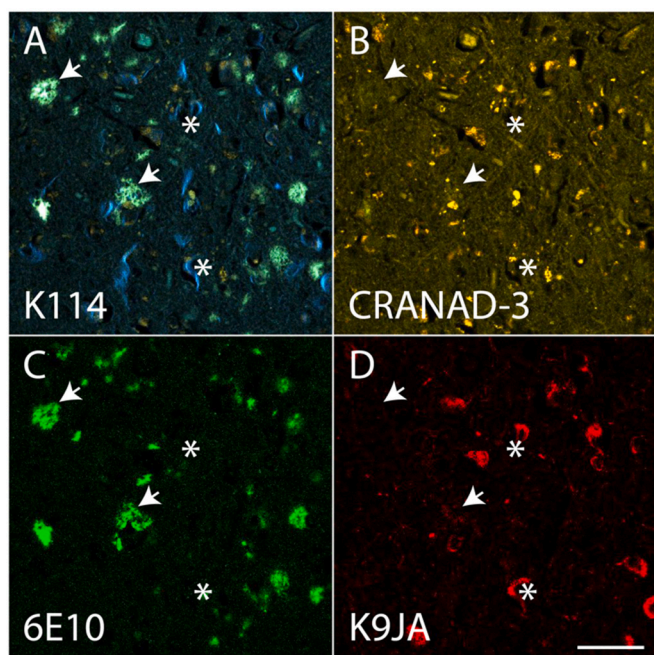
Fig. 10. Comparison of dual probe staining of Aβ plaques and neurofibrillary tangles with immunofluorescence. Abundant amyloid plaque (arrows, green) and tangle pathology (asterisks, blue) revealed by K114 staining (A) is contrasted by the lack of corresponding signal in the CRANAD-3 panel (same field of view, B). Immunohistochemistry performed on the same section (C: anti-amyloid β, D: anti-tau) confirms the protein composition of each deposit. This example further emphasizes the complementary properties of the two probes at reporting not only differences between Aβ plaques, but also tau-rich neurofibrillary tangles. Scale bar: 50 μm. (For interpretation of the references to colour in this figure legend, the reader is referred to the web version of this article.)

utility of the dual-probe approach. While these fluorescent reporters cannot inform on the precise structure of such amyloid deposits, the consistent and complementary nature of the staining provides strong evidence for important differences in the make-up of these aggregates at the nanoscale level.

In human samples, we found that both K114 and CRANAD-3 exhibited preferential binding to different types of aggregates. For instance, we found two distinct K114 emission peaks corresponding to tangles and plaques, confirmed by immunohistochemistry (Fig. 4). Notably, anti-tau immunostaining and tau-associated emission spectrum of K114 were not perfectly correlated, raising questions about the effectiveness of antigen retrieval for revealing the full pathology of protein aggregates. Besides deposits detected by both methods, we noted the presence of tangle-like features that were selectively reported either by anti-tau immunolabeling or by K114 with morphological features and a characteristic blue-shifted spectrum strongly suggesting tau-rich neurofibrillary tangles. We interpret such discrepancies as suggesting that some tangles were aggregated but had not yet "matured" with high β-sheet content (immunopositive but K114-negative) vs. others that are highly aggregated so that even our antigen retrieval steps did not allow antibody penetration (immunonegative but K114-positive). Together these two approaches indicate marked structural heterogeneity of neurofibrillary tangles. Finally, the combination of K114 and CRANAD-3 staining not only surpassed the sensitivity of anti-amyloid β immunolabeling, but also provided rich spectral information, by virtue of inter- and intra-plaque spectral differences (K114) as well as differential binding to particular protein aggregates (CRANAD-3). This gain in sensitivity came without an increase in technical complexity, requiring a simple staining procedure without antigen retrieval, blocking, etc.

In addition to providing excellent morphological detail, the spectral variance yielded reliable quantitative information about the underlying protein aggregates, with different species occupying defined spectral positions (e.g. Aβ vs. tau, Fig. 5, or vascular vs parenchymal amyloid, Fig. 6). A challenge arises from the richness of spectral information requiring novel analytical methods that could yield objective information about the underlying amyloid content. Spectral Scatter Analysis (SSA) allowed for quantitative assessment of both the degree and the types of protein aggregate deposition reported by the dyes used in our study, providing greater insight into the accumulation of misfolded protein pathology in both gray and white matter. For instance, the analysis in Fig. 7 revealed that both control and AD gray matter exhibited high intensity K114-dependent staining, but the prevalence of such signals was both more frequent in AD owing to higher plaque load, and exhibited a different spectral distribution. This suggests not only a difference in the amount of amyloid deposition, but also in the character of accumulated protein aggregates (Zhang et al., 2013). This is further underscored by the strikingly greater spectral variance in AD (Fig. 7H) hinting at the intriguing possibility that normally aging brain accumulates a more homogeneous age-related (presumably less toxic) amyloid, whereas AD gray matter harbors not only a greater amyloid load, but also a much larger variety of (some presumably pathogenic) aggregates. Thus, although cognitively normal cases are known for accumulating cerebral amyloid (Dickson et al., 1992; Piccini et al., 2005), one could speculate based on our results and previously published studies that the structural organization of these aggregates is fundamentally different compared to the conformations present in amyloid plaques and neurofibrillary tangles of AD cases (Zhang et al., 2013; Price and Morris, 1999). Using the differences in K114 emission signatures as a proxy of conformational heterogeneity of Aβ deposits, our findings could be viewed as further evidence for the strain variability hypothesis (Lau et al., 2020), with different conformers arising in controls vs AD brain, or different conformers arising at different stages over time, with the AD disease state potentially promoting a more rapid accumulation of pathogenic species than would occur with regular aging. While the amyloid hypothesis has been questioned due in part to the observation that non-AD cases may also accumulate substantial amyloid load, based on the above we would argue that the molecular makeup, rather that sheer quantity, of the deposited amyloid is an important factor in distinguishing cognitively intact and AD cases. Finally, while subtle Aβ deposition has been reported in AD white matter (Collins-Praino et al., 2014), we were surprised to see the degree to which this was the case when analyzed using our methods (Fig. 7C2). Because detection of AD pathology by conventional means is largely dependent on identification of characteristic amyloid plaques on morphological grounds, the fact that such plaques were rarely seen in white matter would likely result in a substantial underestimate of amyloid load in this region. This surprisingly robust white matter amyloid accumulation might be directly toxic to myelinated axons and could underpin a primary white matter injury that is not merely due to Wallerian degeneration from adjacent gray matter atrophy or from concomitant subcortical microangiopathic pathology (Esparza et al., 2013; de la Monte, 1989). This notion is further supported by a specific microglial activation in AD white matter (Salat et al., 2010; Gouw et al., 2008) suggesting an underlying primary pathological process that is difficult to detect using conventional means.

In conclusion, we report a method that combines two amyloid dyes from different chemical families, K114 and CRANAD-3, to increase the ability to quantitatively detect a broader array of misfolded protein pathology in a tissue section. As we have previously shown, the Congo Red derivative K114 exhibits great spectral variability when bound to different types of amyloid deposits (Stepanchuk et al., 2021), which was confirmed and extended in this study. Importantly, what we show here is that properly selected dye combinations can provide sensitive and highly complementary readouts of amyloid pathology, with a single probe providing only an incomplete picture of the true degree of misfolded protein accumulation. Because these probes reported not only by changes in intensity, but more importantly by spectral shifts, analysis of such spectral images using SSA provided reliable and highly quantitative

measures of amyloid accumulation, even in regions traditionally considered to have only sparse amyloid pathology such as subcortical white matter. Our quantitative metrics hinted at intriguing and possibly fundamental differences in the character of amyloid deposition between aged control and AD brain, indicating that such fluorescence spectroscopic techniques will be useful and powerful tools for exploring the pathobiology of protein misfolding disorders.

Author contribution

AAS and PKS conceived of the work. AAS performed the experiments and data analysis. PKS wrote the analysis software. TL and JTJ provided samples and neuropathological interpretation. PAB, TL and JTJ provided advice on data interpretation. All authors contributed to the writing of the manuscript.

Disclosure of interest

The authors declare no conflict of interest.

Appendix A

Table A.1
Demographic data of cases used in this study.

| Case number	PM delay	AAO	AAD	Duration	Gender	Clinical Diag	Path Diag	Thal Phase	Braak and Braak stage	CERAD	ABC score	CAA	ApoE	TDP-43 pathology	α-syn pathology
P1	16	51	63	12	F	AD	AD	5	6	3	A3B3C3	1	34	0	Neocortical
P2	88.15	63	74	11	M	CBD/PD	AD	4	5	2	A3B3C2	1	33	0	Neocortical
P3	78.15	69	81	12	M	AD	AD	5	6	3	A3B3C3	2	33	Stage 2	0
P4	44	59	75	16	M	PICK'S	AD	5	5	3	A3B3C3	1	34	Stage 1	Neocortical
P5	46.58	65	70	5	F	AD	AD	5	5	3	A3B3C3	0	33	Stage 1	Amygdala
P6	62.1	68	80	12	M	VASC DEM	AD	6	6	3	A3B3C3	1	34	0	Neocortical
P7	88.5	N/A	79	N/A	F	Control	Control	2	1	1	A2B1C1	0	33	0	0
P8	51.4	N/A	87	N/A	F	Control	Control	1	1	0	A1B1C0	0	33	0	0
P9	171	N/A	69	N/A	M	Control	Control	3	1	1	A2B1C1	0	33	0	0
P10	78.5	N/A	85	N/A	M	Control	Control	0	0	0	A0B0C0	0	33	0	0
P11	80.35	N/A	38	N/A	M	Control	Control	1	0	0	A1B0C0	0	34	0	0
P12	87.5	N/A	92	N/A	F	Control	Control	3	3	1	A2B2C1	0	44	0	0
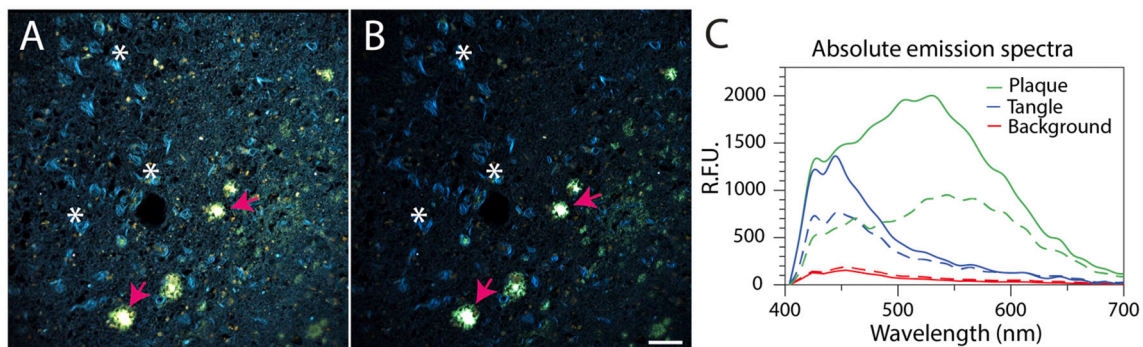
Fig. A.1. K114-stained human AD brain samples before and after exposure to high laser power. Human AD section stained with K114 before (A) and after (B) high intensity laser irradiation (plaques - pink arrows, tangles - asterisks). The absolute emission spectra of plaques, tangles and the background parenchyma before (dashed) and after (solid) photoconversion protocol are shown in panel C. Both β-sheet-rich amyloid plaques and tangles underwent significant fluorescence enhancement after high intensity laser exposure together with a blue-shift of their emission spectra. This is due to a unique photophysical property of amyloid dyes containing Br atoms (Stepanchuk et al., 2021). The overall fluorescence intensity from the background tissue became weaker after photoconversion. The imaging paradigm used for increasing fluorescence of amyloid-bound K114 resulted in better contrast and separation of protein aggregates from the greater tissue parenchyma, decreasing the influence of autofluorescence (including lipofuscin) on spectral analysis of K114 stained samples. Scale bar: 50 μm. (For interpretation of the references to colour in this figure legend, the reader is referred to the web version of this article.)
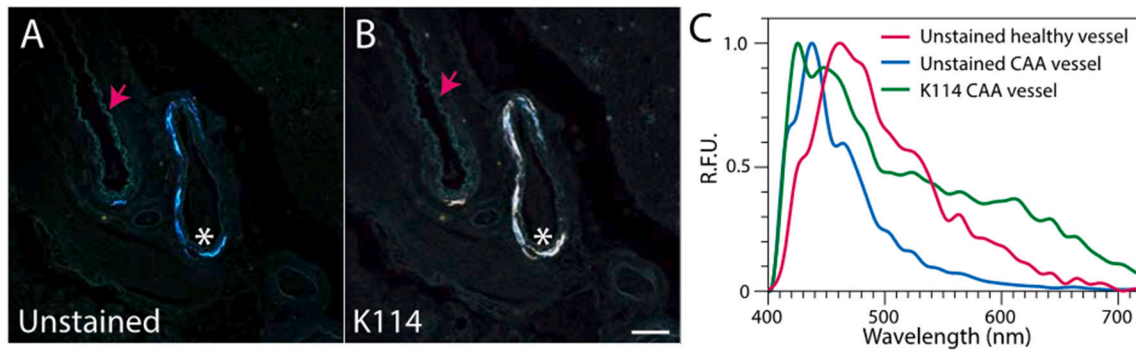
Fig. A.2. Human AD brain vessel sample before and after staining with K114. Prior to staining, the vessels in human AD sections (A) exhibited distinct auto-fluorescence signatures. The vessel with putative cerebral amyloid angiopathy (white asterisk) had a significantly blue-shifted emission spectrum compared to a normal vessel (pink arrow). The features with blue-shifted autofluorescence subsequently exhibited high K114 fluorescence (B), confirming their amyloid nature. Normalized emission spectra are shown in panel C. Scale bar: 50 μm. (For interpretation of the references to colour in this figure legend, the reader is referred to the web version of this article.)
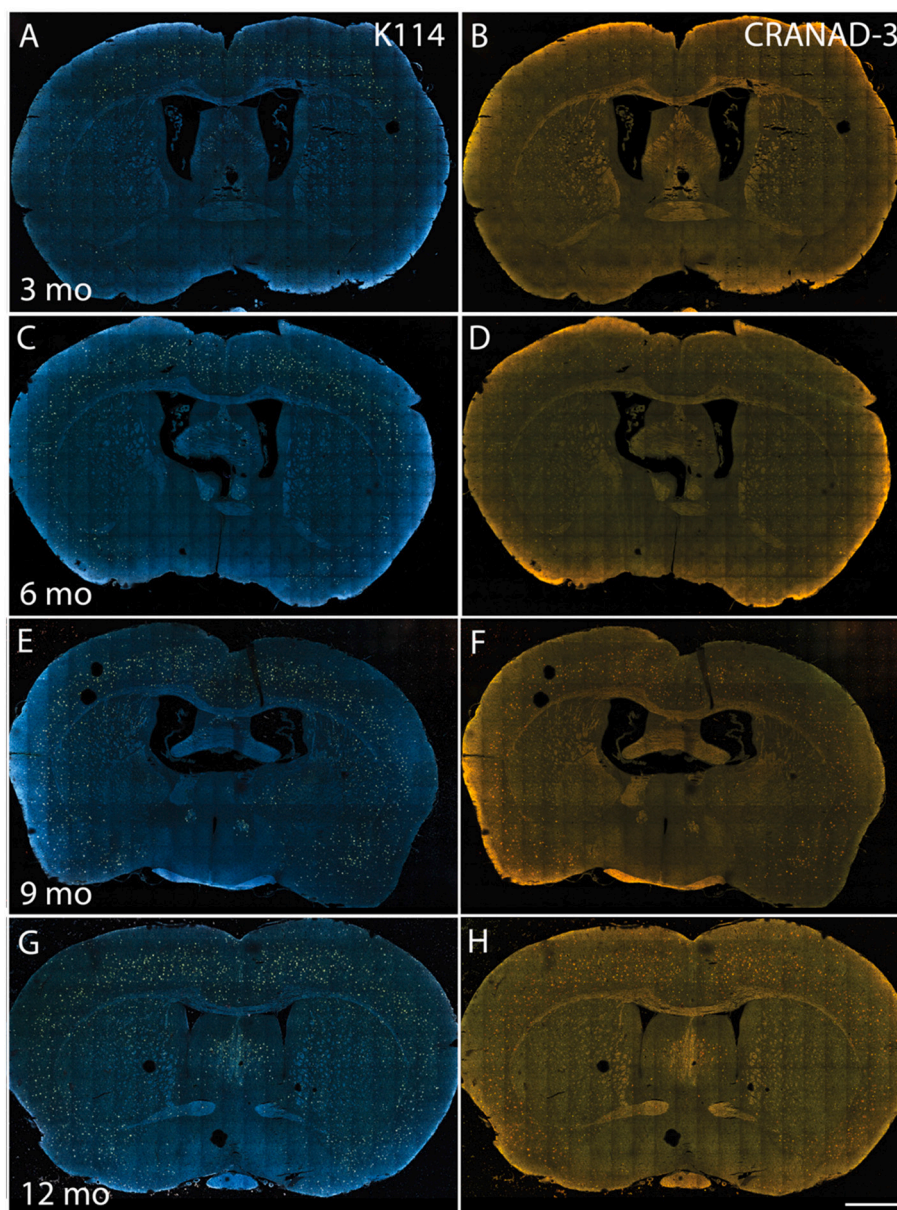

Fig. A.3. Whole brain images of K114 and CRANAD-3-stained sections from 5xFAD mouse. 5xFAD Alzheimer's mouse model exhibits a characteristic increase of plaque load with age. The progression of plaque deposition was evident across 3-, 6-, 9- and 12-months old sections, stained with K114 (A, C, E, G) and CRANAD-3 (C, D, F, H). Scale bar: 1 mm.
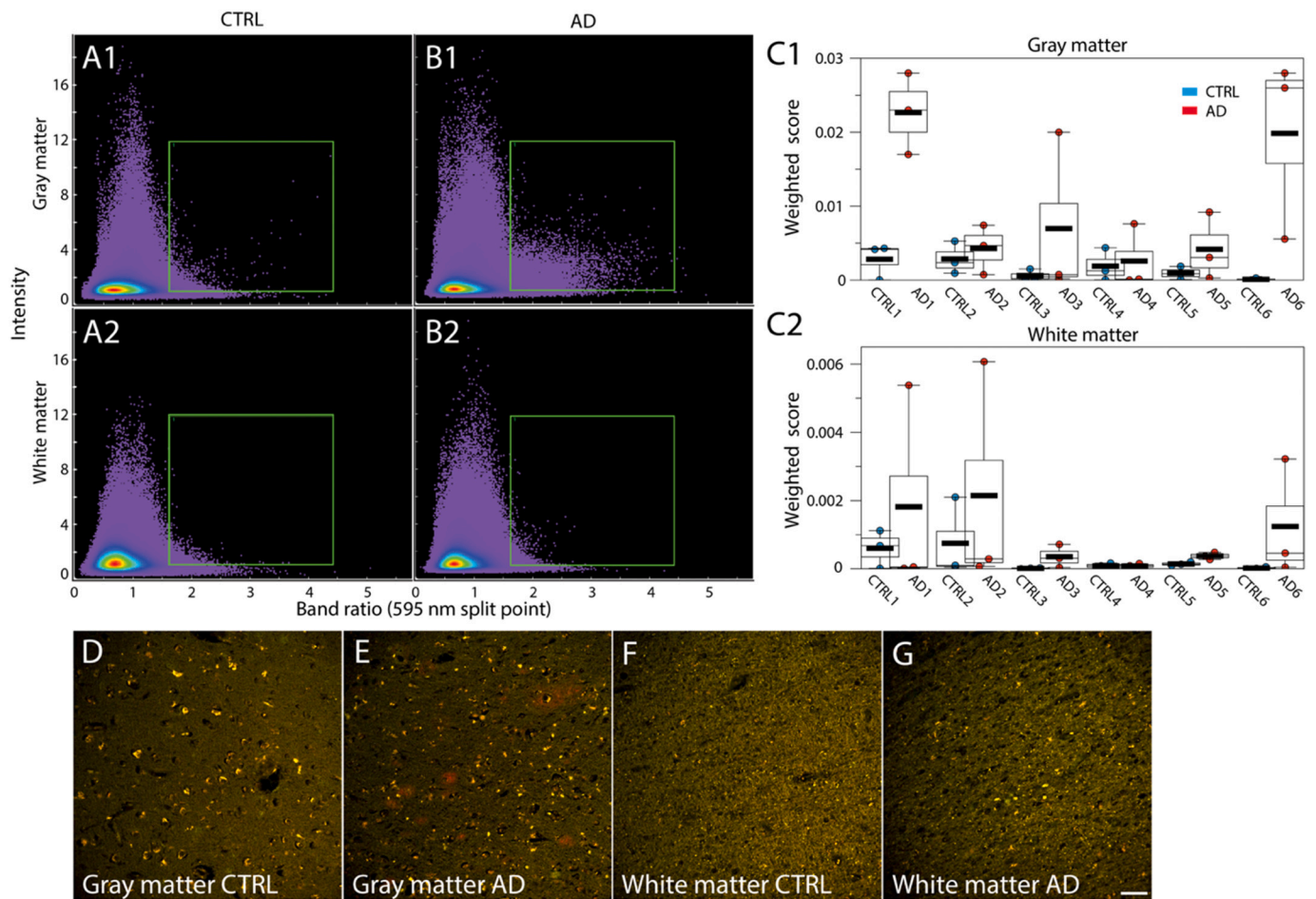
Fig. A.4. CRANAD-3 Spectral Scatter Analysis of human brain samples. Quantitative analysis of CRANAD-3-stained human brain sections. A1-B2 represent aggregate Spectral Scatter Analysis of gray and white matter of all control and AD samples ($N = 6$ subjects in each group). Comparing the pooled SSAs, only gray matter from AD cases exhibited red- shifted kernels of moderate intensity. Mirroring the region of interest (ROI, green rectangle) enclosing these kernels across all SSA graphs resulted in highly variable weighted scores for gray (C1) and white matter (C2) in AD cases (representative images D-G), with a lower variability in control. This contrasted with K114 labeling which yielded very distinct populations that allowed clear separation between controls and AD samples (Fig. 7). Though infrequent compared to K114-positive amyloid deposits, the diffuse red-shifted Aβ aggregates in the AD gray matter (E) were only detected by CRANAD-3 and, to a lesser extent, by immunohistochemistry. Scale bar: 50 μm. (For interpretation of the references to colour in this figure legend, the reader is referred to the web version of this article.)

References

Aliyan, A., Cook, N.P., Martí, A.A., 2019 Nov. Interrogating amyloid aggregates using fluorescent probes. Chem. Rev. https://doi.org/10.1021/acs.chemrev.9b00404 acs. chemrev.9b00404. Available from:

Aoyagi, A., Condello, C., Stöhr, J., Yue, W., Rivera, B.M., Lee, J.C., et al., 2019 May 1. Aβ and tau prion-like activities decline with longevity in the Alzheimer's disease human brain. Sci. Transl. Med. 11 (490), eaat8462. Available from: http://stm.sciencemag.org/content/11/490/eaat8462.abstract.

Armstrong, R.A., Cairns, N.J., Myers, D., Smith, C.U.M., Lantos, P.L., Rossor, M.N., 1996. A comparison of β-amyloid deposition in the medial temporal lobe in sporadic Alzheimer's disease, Down's syndrome and normal elderly brains. Neurodegeneration 5 (1), 35–41.

Arnold, S.E., Hyman, B.T., Flory, J., Damasio, A.R., Van Hoesen, G.W., 1991. The topographical and neuroanatomical distribution of neurofibrillary tangles and neuritic plaques in the cerebral cortex of patients with Alzheimer's disease. Cereb. Cortex 1 (1), 103–116.

Aslund, A., Sigurdson, C.J., Klingstedt, T., Grathwohl, S., Bolmont, T., Dickstein, D.L., et al., 2009 Aug. Novel pentameric thiophene derivatives for in vitro and in vivo optical imaging of a plethora of protein aggregates in cerebral amyloidoses. ACS Chem. Biol. 4 (8), 673–684.

Attems, J., Toledo, J.B., Walker, L., Gelpi, E., Gentleman, S., Halliday, G., et al., 2021. Neuropathological consensus criteria for the evaluation of Lewy pathology in post-mortem brains: a multi-Centre study. Acta Neuropathol. 141, 159–172.

Bennhold, H., 1922. Eine spezifische Amyloidfarbung mit Kongorot. Muenchener Medizinische Wochenschrift 69, 1537–1541.

Biancalana, M., Koide, S., 2010 Jul. Molecular mechanism of Thioflavin-T binding to amyloid fibrils. Biochim. Biophys. Acta 1804 (7), 1405–1412. Available from: https://www.ncbi.nlm.nih.gov/pubmed/20399286.

Braak, H., Braak, E., 1991. Neuropathological stageing of Alzheimer-related changes. Acta Neuropathol. 82 (4), 239–259.

Brelstaff, J., Ossola, B., Neher, J.J., Klingstedt, T., Nilsson, K.P.R., Goedert, M., et al., 2015 May 29. The fluorescent pentameric oligothiophene pFTAA identifies filamentous tau in live neurons cultured from adult P301S tau mice. Front. Neurosci. 9, 184. Available from: https://doi.org/10.3389/fnins.2015.00184.

Burré, J., Sharma, M., Südhof, T.C., 2015 Apr 1. Definition of a molecular pathway mediating α-synuclein neurotoxicity. J. Neurosci. 35 (13), 5221 LP – 5232. Available from: http://www.jneurosci.org/content/35/13/5221.abstract.

Cao, K.J., Elbel, K.M., Cifelli, J.L., Cirera, J., Sigurdson, C.J., Paesani, F., et al., 2018. Solvation-guided design of fluorescent probes for discrimination of amyloids. Sci. Rep. 8 (1), 1–13.

Chu, T.-H., Cummins, K., Sparling, J.S., Tsutsui, S., Brideau, C., Nilsson, K.P.R., et al., 2017 Nov 27. Axonal and myelinic pathology in 5xFAD Alzheimer's mouse spinal cord. PLoS One 12 (11), e0188218. Available from: https://doi.org/10.1371/journal.pone.0188218.

Cline, E.N., Bicca, M.A., Viola, K.L., Klein, W.L., 2018. The amyloid-β oligomer hypothesis: beginning of the third decade. J. Alzheimers Dis. 64 (s1), S567–S610.

Cohen, A.S., Calkins, E., 1959 Apr. Electron microscopic observations on a fibrous component in amyloid of diverse origins. Nature 183 (4669), 1202–1203.

Cohen, M.L., Kim, C., Haldiman, T., ElHag, M., Mehndiratta, P., Pichet, T., et al., 2015 Apr. Rapidly progressive Alzheimer's disease features distinct structures of amyloid-β. Brain 138 (Pt 4), 1009–1022.

Cohen, M., Appleby, B., Safar, J.G., 2016 Jan 25. Distinct prion-like strains of amyloid beta implicated in phenotypic diversity of Alzheimer's disease. Prion 10 (1), 9–17. Available from. https://www.ncbi.nlm.nih.gov/pubmed/26809345.

Collins-Praino, L.E., Francis, Y.I., Griffith, E.Y., Wiegman, A.F., Urbach, J., Lawton, A., et al., 2014 Aug. Soluble amyloid beta levels are elevated in the white matter of Alzheimer's patients, independent of cortical plaque severity. Acta Neuropathol. Commun. 2, 83.

Condello, C., Lemmin, T., Stöhr, J., Nick, M., Wu, Y., Maxwell, A.M., et al., 2018 Jan 23. Structural heterogeneity and intersubject variability of Aβ in familial and sporadic Alzheimer's disease. Proc. Natl. Acad. Sci. U. S. A. 115 (4), E782–E791. Available from. https://www.ncbi.nlm.nih.gov/pubmed/29311311.

Crystal, A.S., Giasson, B.I., Crowe, A., Kung, M.P., Zhuang, Z.P., Trojanowski, J.Q., et al., 2003. A comparison of amyloid fibrillogenesis using the novel fluorescent compound K114. J. Neurochem. 86 (6), 1359–1368.

de la Monte, S.M., 1989 May 1. Quantitation of cerebral atrophy in preclinical and end-stage Alzheimer's disease. Ann. Neurol. 25 (5), 450–459. Available from. https://doi.org/10.1002/ana.410250506.

Dickson, D.W., Crystal, H.A., Mattiace, L.A., Masur, D.M., Blau, A.D., Davies, P., et al., 1992. Identification of normal and pathological aging in prospectively studied nondemented elderly humans. Neurobiol. Aging 13 (1), 179–189.

Esparza, T.J., Zhao, H., Cirrito, J.R., Cairns, N.J., Bateman, R.J., Holtzman, D.M., et al., 2013 Jan 1. Amyloid- beta oligomerization in Alzheimer dementia versus high-pathology controls. Ann. Neurol. 73 (1), 104–119. Available from: https://doi.org/10.1002/ana.23748.

Fändrich, M., Nyström, S., Nilsson, K.P.R., Böckmann, A., LeVine III, H., Hammarström, P., 2018 Mar 1. Amyloid fibril polymorphism: a challenge for molecular imaging and therapy. J. Intern. Med. 283 (3), 218–237. Available from. https://doi.org/10.1111/joim.12732.

Gaspar, R.C., Villarreal, S.A., Bowles, N., Hepler, R.W., Joyce, J.G., Shughrue, P.J., 2010. Oligomers of β-amyloid are sequestered into and seed new plaques in the brains of an AD mouse model. Exp. Neurol. 223 (2), 394–400. Available from: http://www.sciencedirect.com/science/article/pii/S0014488609003720.

Gouw, A.A., Seewann, A., Vrenken, H., van der Flier, W.M., Rozemuller, J.M., Barkhof, F., et al., 2008 Dec. Heterogeneity of white matter hyperintensities in Alzheimer's disease: post-mortem quantitative MRI and neuropathology. Brain 131 (Pt 12), 3286–3289.

Gravina, S.A., Ho, L., Eckman, C.B., Long, K.E., Otvos, L.J., Younkin, L.H., et al., 1995 Mar. Amyloid beta protein (A beta) in Alzheimer's disease brain. Biochemical and immunocytochemical analysis with antibodies specific for forms ending at A beta 40 or A beta 42(43). J. Biol. Chem. 270 (13), 7013–7016.

Greenberg, S.M., Bacskai, B.J., Hernandez-Guillamon, M., Pruzin, J., Sperling, R., van Veluw, S.J., 2020 Jan. Cerebral amyloid angiopathy and Alzheimer disease - one peptide, two pathways. Nat. Rev. Neurol. 16 (1), 30–42.

Hammarström, P., Simon, R., Nyström, S., Konradsson, P., Åslund, A., KPR, Nilsson, 2010 Aug 17. A fluorescent pentameric thiophene derivative detects in vitro-formed prefibrillar protein aggregates. Biochemistry 49 (32), 6838–6845. Available from. https://doi.org/10.1021/bi100922r.

Holmes, B.B., Diamond, M.I., 2014 Jul. Prion-like properties of Tau protein: the importance of extracellular Tau as a therapeutic target. J. Biol. Chem. 289 (29), 19855–19861.

Howie, A.J., Brewer, D.B., 2009. Optical properties of amyloid stained by Congo red: history and mechanisms. Micron. 40 (3), 285–301.

Howie, A.J., Owen-Casey, M.P., 2010. Discrepancies between descriptions and illustrations of colours in Congo red-stained amyloid, and explanation of discrepant colours. Amyloid 17 (3–4), 109–117.

Howie, A.J., Brewer, D.B., Howell, D., Jones, A.P., 2008. Physical basis of colors seen in Congo red-stained amyloid in polarized light. Lab. Investig. 88 (3), 232–242.

Iwamoto, N., Nishiyama, E., Ohwada, J., Arai, H., 1997. Distribution of amyloid deposits in the cerebral white matter of the Alzheimer's disease brain: relationship to blood vessels. Acta Neuropathol. 93 (4), 334–340. Available from: https://doi.org/10.1007/s004010050624.

Josephs, K.A., Murray, M.E., Whitwell, J.L., Tosakulwong, N., Weigand, S.D., Petrucelli, L., Liesinger, A.M., Petersen, R.C., Parisi, J.E., Dickson, D.W., 2016 Apr. Updated TDP-43 in Alzheimer's disease staging scheme. Acta Neuropathol. 131 (4), 571–585.

Jucker, M., Walker, L.C., 2018 Oct. Propagation and spread of pathogenic protein assemblies in neurodegenerative diseases. Nat. Neurosci. 21 (10), 1341–1349.

Khurana, R., Coleman, C., Ionescu-Zanetti, C., Carter, S.A., Krishna, V., Grover, R.K., et al., 2005. Mechanism of thioflavin T binding to amyloid fibrils. J. Struct. Biol. 151 (3), 229–238. Available from: http://www.sciencedirect.com/science/article/pii/S1047847705001309.

Kollmer, M., Close, W., Funk, L., Rasmussen, J., Bsoul, A., Schierhorn, A., et al., 2019. Cryo-EM structure and polymorphism of Aβ amyloid fibrils purified from Alzheimer's brain tissue. Nat. Commun 10 (1), 4760. Available from: https://doi.org/10.1038/s41467-019-12683-8.

Lam, B., Masellis, M., Freedman, M., Stuss, D.T., Black, S.E., 2013. Clinical, imaging, and pathological heterogeneity of the Alzheimer's disease syndrome. Alzheimers Res. Ther. 5 (1), 1. Available from: https://doi.org/10.1186/alzrt155.

Langer, F., Eisele, Y.S., Fritschi, S.K., Staufenbiel, M., Walker, L.C., Jucker, M., 2011 Oct 12. Soluble Aβ seeds are potent inducers of cerebral β-amyloid deposition. J. Neurosci. 31 (41), 14488–14495. Available from: http://www.jneurosci.org/content/31/41/14488.abstract.

Lau, H.H.C., Lau, A., Watts, J.C., 1777. Discriminating strains of self-propagating protein aggregates using a conformational stability assay. Methods Mol. Biol. 2018, 339–354.

Lau, H.H.C., Ingelsson, M., Watts, J.C., 2020. The existence of Aβ strains and their potential for driving phenotypic heterogeneity in Alzheimer's disease. Acta Neuropathol. https://doi.org/10.1007/s00401-020-02201-2. Available from:

Levine, H., 2005. Mechanism of A (1–40) Fibril-Induced Fluorescence of (trans, trans)-1-Bromo-2, 5-bis (4-hydroxystyryl) Benzene (K114), pp. 15937–15943.

Magnusson, K., Simon, R., Sjölander, D., Sigurdson, C.J., Hammarström, P., Nilsson, K.P. R., 2014. Multimodal fluorescence microscopy of prion strain specific PrP deposits stained by thiophene-based amyloid ligands. Prion 8 (4), 319–329. Available from: https://www.ncbi.nlm.nih.gov/pubmed/25495506.

Meyer-Luehmann, M., Coomaraswamy, J., Bolmont, T., Kaeser, S., Schaefer, C., Kilger, E., et al., 2006 Sep 22. Exogenous induction of cerebral β-amyloidogenesis is governed by agent and host. Science 313 (5794), 1781–1784. Available from: http://science.sciencemag.org/content/313/5794/1781.abstract.

Nesterov, E.E., Skoch, J., Hyman, B.T., Klunk, W.E., Bacskai, B.J., Swager, T.M., 2005 Aug 22. In vivo optical imaging of amyloid aggregates in brain: design of fluorescent markers. Angew. Chem. Int. Ed. 44 (34), 5452–5456. Available from. https://doi.org/10.1002/anie.200500845.

Nilsson, K.P.R., Lindgren, M., Hammarström, P., 2018. In: Sigurdsson, E.M., Calero, M., Gasset, M. (Eds.), Luminescent-Conjugated Oligothiophene Probe Applications for Fluorescence Imaging of Pure Amyloid Fibrils and Protein Aggregates in Tissues BT - Amyloid Proteins: Methods and Protocols. Springer New York, New York, NY, pp. 485–496. Available from: https://doi.org/10.1007/978-1-4939-7816-8_30.

Piccini, A., Russo, C., Gliozzi, A., Relini, A., Vitali, A., Borghi, R., et al., 2005. β-Amyloid is different in normal aging and in Alzheimer disease. J. Biol. Chem. 280 (40), 34186–34192. Available from: https://www.sciencedirect.com/science/article/pii/s0021925820790071.

Price, J.L., Morris, J.C., 1999 Mar. Tangles and plaques in nondemented aging and "preclinical" Alzheimer's disease. Ann. Neurol. 45 (3), 358–368.

Prusiner, S.B., 2012. A unifying role for prions in neurodegenerative diseases. In: Science, 336. American Association for the Advancement of Science, pp. 1511–1513.

Ran, C., Moore, A., 2012 Jun. Spectral unmixing imaging of wavelength-responsive fluorescent probes: an application for the real-time report of amyloid Beta species in Alzheimer's disease. Mol. Imaging Biol. 14 (3), 293–300.

Reinke, A.A., Gestwicki, J.E., 2011 Jun 1. Insight into amyloid structure using chemical probes. Chem. Biol. Drug Des. 77 (6), 399–411. Available from. https://doi.org/10.1111/j.1747-0285.2011.01110.x.

Reitz, C., 2012. Alzheimer's disease and the amyloid cascade hypothesis: a critical review. Int. J. Alzheimers Dis. 2012, 369808. Available from: https://doi.org/10.1155/2012/369808.

Rodrigue, K.M., Kennedy, K.M., Park, D.C., 2009. Beta-amyloid deposition and the aging brain. Neuropsychol. Rev. 19 (4), 436–450.

Salat, D.H., Tuch, D.S., van der Kouwe, A.J.W., Greve, D.N., Pappu, V., Lee, S.Y., et al., 2010 Feb. White matter pathology isolates the hippocampal formation in Alzheimer's disease. Neurobiol. Aging 31 (2), 244–256.

Sengupta, U., Nilson, A.N., Kayed, R., 2016. The role of amyloid-β oligomers in toxicity, propagation, and immunotherapy. EBioMedicine 6, 42–49. Available from: http://www.sciencedirect.com/science/article/pii/S2352396416301219.

Serrano-Pozo, A., Frosch, M.P., Masliah, E., Hyman, B.T., 2011 Sep. Neuropathological alterations in Alzheimer disease. Cold Spring Harb. Perspect. Med. 1 (1), a006189.

Shewmaker, F., McGlinchey, R.P., Wickner, R.B., 2011 May 13. Structural insights into functional and pathological amyloid. J. Biol. Chem. 286 (19), 16533–16540. Available from: https://pubmed.ncbi.nlm.nih.gov/21454545.

Sigurdson, C.J., Nilsson, K.P.R., Hornemann, S., Manco, G., Polymenidou, M., Schwarz, P., et al., 2007 Dec 18. Prion strain discrimination using luminescent conjugated polymers. Nat. Methods 4 (12), 1023–1030 [cited 2019 Mar 17]. Available from: http://www.nature.com/articles/nmeth1131.

Stepanchuk, A., Tahir, W., Nilsson, K.P.R., Schatzl, H.M., Stys, P.K., 2020 Aug 16. Early detection of prion protein aggregation with a fluorescent pentameric oligothiophene probe using spectral confocal microscopy. J. Neurochem. https://doi.org/10.1111/jnc.15148. Available from:

Stepanchuk, A.A., Heyne, B., Stys, P.K., 2021 Mar 11. Complex photophysical properties of K114 make for a versatile fluorescent probe for amyloid detection. ACS Chem. Neurosci. https://doi.org/10.1021/acschemneuro.1c00101. Available from:

Styren, Scot D., Hamilton, R.L., Styren, G.C., Klunk, W.E., 2000 Sep 1. X-34, a fluorescent derivative of congo red: a novel histochemical stain for Alzheimer's disease pathology. J. Histochem. Cytochem. 48 (9), 1223–1232. Available from. https://doi.org/10.1177/002215540004800906.

Thal, D.R., Rüb, U., Orantes, M., Braak, H., 2002 Jun. Phases of A beta-deposition in the human brain and its relevance for the development of AD. Neurology 58 (12), 1791–1800.

Toomey, C.E., Heywood, W., Benson, B.C., Packham, G., Mills, K., Lashley, T., 2020 Jul. Investigation of pathology, expression and proteomic profiles in human TREM2 variant postmortem brains with and without Alzheimer's disease. Brain Pathol. 30 (4), 794–810. https://doi.org/10.1111/bpa.12842. Epub 2020 Apr 29. 32267026.

Vaz, M., Silvestre, S., 2020 Nov. Alzheimer's disease: recent treatment strategies. Eur. J. Pharmacol. 887, 173554.

Verwilst, P., Kim, H.S., Kim, S., Kang, C., Kim, J.S., 2018. Shedding light on tau protein aggregation: the progress in developing highly selective fluorophores. Chem. Soc. Rev. 47 (7), 2249–2265. Available from: https://doi.org/10.1039/C7CS00706J.

Villain, N., Dubois, B., 2019 Apr. Alzheimer's disease including focal presentations. Semin. Neurol. 39 (2), 213–226.

Watts, J.C., Condello, C., Stöhr, J., Oehler, A., Lee, J., DeArmond, S.J., et al., 2014 Jul. Serial propagation of distinct strains of Aβ prions from Alzheimer's disease patients. Proc. Natl. Acad. Sci. U. S. A. 111 (28), 10323–10328.

Zhang, X., Tian, Y., Li, Z., Tian, X., Sun, H., Liu, H., et al., 2013 Nov 6. Design and synthesis of curcumin analogues for in vivo fluorescence imaging and inhibiting

copper-induced cross-linking of amyloid beta species in Alzheimer's disease. J. Am. Chem. Soc. 135 (44), 16397–16409. Available from. https://doi.org/10.1021/ja405239v.

Zhang, X., Tian, Y., Zhang, C., Tian, X., Ross, A.W., Moir, R.D., et al., 2015 Aug. Near-infrared fluorescence molecular imaging of amyloid beta species and monitoring therapy in animal models of Alzheimer's disease. PNAS 112 (31), 9734–9739. Available from: https://doi.org/10.1073/pnas.1505420112.

Zhang, J., Sandberg, A., Konsmo, A., Wu, X., Nyström, S., Nilsson, K.P.R., et al., 2018 May. Detection and imaging of Aβ1-42 and tau fibrils by redesigned fluorescent X-34 analogues. Chemistry 24 (28), 7210–7216.

Zhou, K., Yuan, C., Dai, B., Wang, K., Chen, Y., Ma, D., et al., 2019 Jul 25. Environment-sensitive near- infrared probe for fluorescent discrimination of Aβ and tau fibrils in AD brain. J. Med. Chem. 62 (14), 6694–6704. Available from: https://doi.org/10.1021/acs.jmedchem.9b00672.